TU/e EINDHOVEN UNIVERSITY OF TECHNOLOGY

Mathematical models of contrast transport kinetics for cancer diagnostic imaging: a review

Citation for published version (APA):
Turco, S., Wijkstra, H., & Mischi, M. (2016). Mathematical models of contrast transport kinetics for cancer diagnostic imaging: a review. *IEEE Reviews in Biomedical Engineering*, *9*, 121-147. https://doi.org/10.1109/RBME.2016.2583541

Document license:
TAVERNE

DOI:
10.1109/RBME.2016.2583541

Document status and date:
Published: 22/06/2016

Document Version:
Publisher's PDF, also known as Version of Record (includes final page, issue and volume numbers)

Please check the document version of this publication:

• A submitted manuscript is the version of the article upon submission and before peer-review. There can be important differences between the submitted version and the official published version of record. People interested in the research are advised to contact the author for the final version of the publication, or visit the DOI to the publisher's website.
• The final author version and the galley proof are versions of the publication after peer review.
• The final published version features the final layout of the paper including the volume, issue and page numbers.

Link to publication

General rights
Copyright and moral rights for the publications made accessible in the public portal are retained by the authors and/or other copyright owners and it is a condition of accessing publications that users recognise and abide by the legal requirements associated with these rights.

• Users may download and print one copy of any publication from the public portal for the purpose of private study or research.
• You may not further distribute the material or use it for any profit-making activity or commercial gain
• You may freely distribute the URL identifying the publication in the public portal.

If the publication is distributed under the terms of Article 25fa of the Dutch Copyright Act, indicated by the "Taverne" license above, please follow below link for the End User Agreement:

www.tue.nl/taverne

Take down policy
If you believe that this document breaches copyright please contact us at:

openaccess@tue.nl

providing details and we will investigate your claim.

Download date: 07. Nov. 2026

Mathematical Models of Contrast Transport Kinetics for Cancer Diagnostic Imaging: A Review

Simona Turco, *Student Member, IEEE*, Hessel Wijkstra, *Senior Member, IEEE*, and Massimo Mischi, *Senior Member, IEEE*

(Methodological Review)

***Abstract*—Angiogenesis plays a fundamental role in cancer growth and the formation of metastasis. Novel cancer therapies aimed at inhibiting angiogenic processes and/or disrupting angiogenic tumor vasculature are currently being developed and clinically tested. The need for earlier and improved cancer diagnosis, and for early evaluation and monitoring of therapeutic response to angiogenic treatment, have led to the development of several imaging methods for *in vivo* noninvasive assessment of angiogenesis. The combination of dynamic contrast-enhanced imaging with mathematical modeling of the contrast agent kinetics enables quantitative assessment of the structural and functional changes in the microvasculature that are associated with tumor angiogenesis. In this paper, we review quantitative imaging of angiogenesis with dynamic contrast-enhanced magnetic resonance imaging, computed tomography, and ultrasound.**

***Index Terms*—Cancer angiogenesis, dynamic-contrast enhanced imaging, indicator dilution theory, pharmacokinetic modeling.**

I. Introduction

THE CRUCIAL role of angiogenesis and vasculogenesis in tumor growth and development is today well established. Angiogenesis is the process through which new blood vessels are formed from preexisting ones, whereas vasculogenesis is the *de novo* formation of vessels from precursor cells. Angiogenesis and vasculogenesis are involved in a number of physiological processes such as wound healing, embryogenesis, and corpus luteum formation, as well as in pathological conditions including psoriasis, age-related macular degeneration, and cancer [1].

In the early stage of cancer development, the tumor is nourished by diffusion of oxygen and nutrients provided by nearby blood vessels [2], [3]. In this phase, referred to as avascular phase, the tumor cannot grow beyond 1–2 mm in diameter [2]–[4]. The transition from a prevascular to a vascularized phase, known as "angiogenic switch," is required for the tumor to overcome this size limit. The process may also be accompanied by lymphangionesis by which the growing tumor can gain access to the lymphatic system through the production of new lymphatic vessels [5], [6]. The increased blood supply provided by neovascularization allows for tumor progression and may also be involved in the formation of metastasis [4], [7]. As a matter of fact, lymphatic and/or blood vessels provide the escape route for tumor cells to enter the systemic circulation and reach other sites and tissues in the body [8], [9]. Eventually, through a complex process involving several events, metastatic tumor cells activate changes in the vascular permeability of blood vessels of target organs and penetrate into the target tissue through extravasation [5].

At a microvascular level, tumor angiogenesis is characterized by an increased number of vessels in a heterogeneous and poorly organized vascular environment. Neoangiogenic vessels differ from normal capillaries, showing a high degree of tortuosity and irregularity. They also exhibit a higher permeability, arteriovenous shunting, chaotic flow patterns, and fragility [2], [3], [7], [10], [11]. These abnormalities in the vascular architecture make the hemodynamic changes in the blood flow more complex to analyze. Lack of vasomotor control and an increase in arteriovenous shunts cause a low flow resistance and an increased blood flow, while the high tortuosity and irregularity, together with the high interstitial pressure due to the extravascular leakage, lead to increased flow resistance, and decreased perfusion [3], [12]–[14].

At a molecular level, tumor angiogenesis may be triggered by hypoxia, acidosis, and hypoglycemia leading to the activation of proangiogenic proteins, such as vascular endothelial growth factors (VEGF) and transforming growth factors, which promote the formation of new capillaries by recruiting, activating, and stimulating endothelial cells [15]. Once activated, endothelial cells secrete matrix metallo-proteases, which degrade the basement membrane, and integrins, which enable their migration into the extracellular matrix toward the tumor [16]. Numerous current therapeutic strategies aim at stopping tumor growth by interfering with various steps in this process. Antiangiogenic drugs may act in the earliest stage of angiogenesis by

Manuscript received October 9, 2015; revised January 20, 2016 and April 19, 2016; accepted May 23, 2016. Date of publication June 22, 2016; date of current version September 16, 2016.

S. Turco and M. Mischi are with the Department of Electrical Engineering, Eindhoven University of Technology, Eindhoven 5600MB, The Netherlands (e-mail: s.turco@tue.nl; m.mischi@tue.nl).

H. Wijkstra is with the Department of Urology, Academic Medical Center, University of Amsterdam, Amsterdam 1105AZ, The Netherlands, and also with the Department of Electrical Engineering, Eindhoven University of Technology, Eindhoven 5600MB, The Netherlands (e-mail: h.wijkstra@tue.nl).

Digital Object Identifier 10.1109/RBME.2016.2583541

1937-3333 © 2016 IEEE. Personal use is permitted, but republication/redistribution requires IEEE permission.
See http://www.ieee.org/publications_standards/publications/rights/index.html for more information.

inhibiting the synthesis of angiogenic proteins by the tumor, or they can intervene later in the process by neutralizing the angiogenic proteins with antibodies and traps, by blocking the binding of angiogenic factors to the endothelial walls, or by direct induction of endothelial cell apoptosis[6].

Advances in this promising area of oncologic research have drawn increasing attention to the development of accurate tools for quantitative assessment of angiogenesis, for tumor diagnosis, therapeutic decision making, and antiangiogenic treatment monitoring [3].

Traditional *in vitro* methods for angiogenesis quantitation include the measurement of circulating angiogenic factors such as endothelial progenitor cells in body fluids [17], [18], and the immunohistochemical analysis of tissue samples to assess the microvasculature density (MVD), which has been correlated with tumor aggressiveness and the risk of metastasis formation [12], [17], [19]–[21]. Following on the protocol first proposed by Weidner *et al.* [21], MVD counting is performed by staining tissue specimens for angiogenesis assays, such as endothelium cells or other vascular wall components, and then analyzing the specimen either manually, through traditional microscopic techniques, or automatically through computer-assisted image analysis methods [22], [23]. However, this approach has several limitations: it is invasive and, hence, not suitable for monitoring treatment; it provides only morphological information on tumor vascularity; it does not provide reliable information on tumor localization and delineation, which is essential for focal therapy guidance [8]; it is affected by random tissue sampling errors and interobserver variability [11], [19], [20], [23].

Alternatively, several imaging modalities offer noninvasive methods for *in vivo* detection of angiogenesis. These include ultrasounds (US), magnetic resonance imaging (MRI), single-photon emission computed tomography, positron emission tomography, and computed tomography (CT) [24]. In general, there are three main approaches to tackle angiogenesis imaging: 1) by direct imaging of molecular expressions of tumor angiogenesis, 2) by looking into metabolic aspects of angiogenesis such as hypoxia and glucose consumption, and 3) by assessing morphological and functional changes in tumor microvasculature and microcirculation [15].

In this review, we focus on the latter approach. Specifically, we review quantitative imaging of angiogenesis with dynamic contrast-enhanced US (DCE-US), MRI (DCE-MRI), and CT (DCE-CT). The enhancement of imaging modalities with the use of contrast media offers greater possibilities for imaging tumor vascularity [2], [25]. The contrast kinetic distribution, and thus the signal enhancement patterns observed in DCE images, depends on several hemodynamic features including regional blood flow and volume, vessel density, and vessel permeability [2]. As a result, DCE imaging offers additional information on organ perfusion and the tumor microenvironment that conventional static imaging fails to provide. Moreover, combining it with physiological modeling allows for the assessment of quantitative parameters that are directly related to the physiological features underlying tumor angiogenesis [24]. We restrict the investigation to DCE-MRI, DCE-US, and DCE-CT because they are widely accessible and they have a well-established user base. Several contrast agents for these modalities have already been cleared for clinical use [26]–[28], and contrast-enhanced imaging protocols are already available or easily implementable in standard clinical settings [2], [29]. The fairly high spatio-temporal resolution allows for the application of physiological models of variable complexity. Moreover, wide-availability, low to reasonable cost, and the absence of ionizing radiation (DCE-US, DCE-MRI) make these modalities very suitable for antiangiogenic therapy monitoring and treatment follow up, whereby several repeated acquisitions are needed. As a result, these modalities are very promising in this exciting research area, with many developments foreseeable in the near future.

After a general introduction on indicator dilution techniques and modeling approaches, we analyze the different contrast-enhanced imaging modalities and the pharmacokinetic models that have been developed. For each modality, we discuss the characteristics of the contrast agent used, we explain the conversion from signal intensity to tissue concentration, we examine models' mathematical formulations and main assumptions, and we highlight the different angiogenic features that they can reflect. Then, we describe the potential clinical applications and we provide an overview of the main clinical studies that have been carried out up until now. Finally, we compare the different imaging modalities, discussing potential advantages and limitations and the outlook for future developments.

II. Pharmacokinetic Modeling of Contrast Agents for Quantitative Imaging of Angiogenesis

The long history of indicator dilution theory started in 1761, when Haller first reported the injection of an indicator into the vena cava of a freshly killed animal to compare pulmonary circulation times through the inflated and collapsed lungs [30], [31]. In these early stages, the main developments and applications of indicator dilution techniques were related to the cardiovascular field. In this context, memorable milestones are the introduction by Hering of the first method to measure blood (volume) flow in 1824, the extension of the method by Stewart for measuring cardiac output (CO) and central blood volume in 1897, and its subsequent correction made by Hamilton to take into account the recirculation of the indicator, leading to the well-known Stewart–Hamilton equation for CO measurement [30], [32]. Starting from the cardiovascular field, the indicator dilution theory framework has been extended to investigate several dynamic biological processes, including production, distribution, transport, and utilization of exogenous drugs or endogenous metabolites.

An indicator dilution technique can thus be generalized as a method used for characterizing the vascular hemodynamic or the metabolic functions of some tissue when a known amount of an indicator substance (i.e., contrast agent) is injected upstream into the circulatory system and its concentration is sampled downstream over time [33], [34].

In general, an indicator is any compound that exhibits the same pharmacokinetic behavior of the substance to be traced, but it can be detected distinctively and it does not perturb the kinetics of the system to a significant extent [35], [36]. Although the words tracer and indicator are often used indistinctively, a tracer is a particular type of indicator which is chemically identical to a systemic substance [37]. Indicators

differs in their chemical and physical properties, and in their interactions and distribution within the body. According to their biodistribution, they can be classified into intravascular tracers, which remain confined in the bloodstream, extravascular extracellular tracers, which leak into the extravascular space but do not enter the cells, and intracellular tracers, which are able to cross the cellular membrane. Of the latter, a further distinction can be made between metabolizable and nonmetabolizible tracers, depending on whether they are digested by the cell or not [38].

The injection of the indicator can be performed either instantaneously, in which case it is referred to as bolus- or delta-function injection, or by infusion at a constant rate, usually referred to as constant infusion injection [32].

The sampling method depends on the nature of the indicator and on the specific application. Traditional indicator dilution measurements are inherently invasive because they require central catheterization in order to produce a series of measurements at the sampling site [31]. After detection, the conversion to time concentration curve is obtained according to the specific tracer and the adopted measurement method. Typical examples in CO measurements include cold thermodilution [31], [39], based on temperature variations at the sampling site due to the passage of a cold indicator, dye dilution [31], in which the concentration changes of a colored dye are measured by means of absorption photometry, and lithium dilution [31], in which changes in the Nerst potential due to the passage of lithium are related to its concentration. Other techniques especially used in pharmacokinetics involve the use of stable or radioactive isotopes of a substance to be traced, whose changes in concentration are evaluated through mass differences or radioactivity measurements, respectively [36].

Indicator dilution curves (IDCs) can also be obtained noninvasively with several contrast-enhanced imaging modalities. In this study, we focus on DCE-US, DCE-MRI, and DCE-CT. The conversion from image intensity to contrast concentration curves is generally attained through dedicated calibration procedures, which differ depending on the specific contrast and imaging method used.

Once the time concentration curves are obtained, data interpretation and quantitative analysis can be achieved by two fundamentally different approaches: data-driven modeling and system-driven modeling [38].

In data-driven modeling, the input–output response is analyzed without making any assumption on the underlying structure generating the experimental data. This can be done either through a model-free approach, by evaluating relevant quantities directly from the experimental data, or through a black-box model approach, by fitting the data to a mathematical expression or by calculating the (model-free) impulse response function through deconvolution. Although the data-driven approaches are independent from *a priori* model structure assumptions and more straightforward to implement, the extracted semiquantitative parameters have no direct relation with the physiology of the system, and thus cannot provide descriptive information about the physiological mechanisms underlying the observed data [40]. However, semiquantitative parameters [41], [42] (see Fig. 1(a); Table I) typically extracted from data-driven approaches may still be related to physiological quantities such as fractional blood volume [peak enhancement (PE)], blood flow [area under the curve (AUC), time to peak (TTP), appearance time (AT), wash-in time (WIT), wash-in rate (WIR), mean transit time (MTT), wash-out time (WOT), wash-out rate (WIR)], and permeability and interstitial volume (WOT, WIR, MTT).

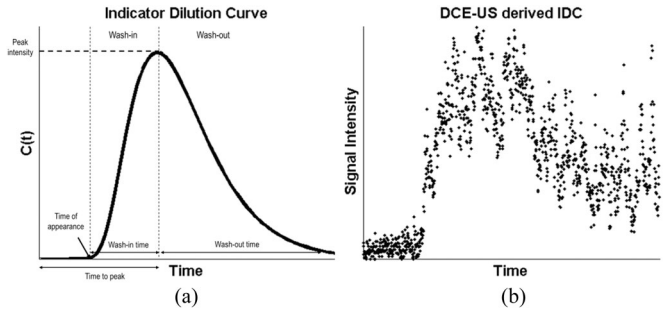

Fig. 1. (a) Theoretical IDC. After a characteristic time of appearance, the curve rises from a baseline value to the peak concentration in the wash-in phase, and decreases back to the baseline level in the wash-out phase. (b) IDC obtained from a DCE-US study. The curve is affected by noise, and the down-slope of the curve is hidden by a rise due to the recirculation of the indicator.

The alternative approach is modeling the system, representing the physiological reality in the form of mathematical equations with a certain degree of approximation [38]. This approach, also referred to as glass-box modeling, offers the advantage that the dynamic behavior of the system can be described and quantified through physiological parameters that are explicitly incorporated into the model. The main approach for system modeling is represented by compartmental modeling, which is widely used to describe transport phenomena in biological systems. Compartmental models decompose a physiological system into a certain number of interacting compartments, each governed by the mass conservation law and described by a system of differential equations [35], [38], [43].

Conventional lumped compartmental models assume the compartments to contain instantaneously well-mixed kinetically-homogenous material, whose concentration is a function of time only. Lumped models are attractive for their simplicity, but they may oversimplify the description of the investigated biological system [40]. Alternatively, distributed models take into account kinetic inhomogeneities, such as concentration gradients within a compartment, by expressing concentrations as a function of spatial location in addition to time, and may lead to a mathematically more complex, but physiologically more accurate description of the system [40]. Once the system structure has been defined, estimation of the parameters can be achieved either by solving the differential equations describing the dilution system, or by studying the impulse response function of each compartment by means of deconvolution methods. In both cases, the assumptions of linearity and time invariance are implicitly made. These imply that the output given by the sum of two inputs is equal to the sum of the outputs given by the separate inputs, and that the parameters of the system are constant during the period of observation [44], [45].

TABLE I
COMMON SEMIQUANTITATIVE PARAMETERS USED IN DCE IMAGING

Semiquantitative parameter	Description	Related to
Area under the curve (AUC)	Time-integral of the IDC	Blood flow, injected dose
Appearance time (AT)	Time of onset of the IDC	Blood flow
Peak enhancement (PE)	Maximum value of the IDC	Blood volume, injected dose
Time to peak (TTP)	Time of PE	Blood flow
Wash-in time (WIT)	Difference between TTP and AT	Blood flow
Wash-in rate (WIR)	Gradient of the wash-in	Blood flow
Wash-out time (WOT)	Time between PE and the time at which the curve returns to baseline (often extrapolated from fitting)	Blood flow, capillary permeability, interstitial volume
Wash-out rate (WIR)	Gradient of the wash-out	Blood flow, capillary permeability, interstitial volume

Finally, based on the nature of the model variables, a further distinction can be made between statistical models, in which one or more variables are stochastic variables, and deterministic models, in which all the variables can be predicted in any position at any time [35], [38].

In the following paragraphs, indicator dilution modeling with DCE-US, DCE-MRI, and DCE-CT are analyzed in detail, describing contrast agent properties, discussing aspects of signal intensity to tracer concentration conversion, and providing an overview of the mathematical models available for quantitative analysis of the hemodynamic and functional features of tumor angiogenesis.

A. Intravascular Contrast Agents: DCE-US

1) Contrast Agent Properties and Signal Calibration: US contrast agents (UCAs) are solutions of air-filled or gas-filled elastic microbubbles with mean diameter in the range of 1–7 μm [46]–[48]. Due to their size, which is smaller than red blood cells (6–8 μm), they are suitable for intravenous injection and they can circulate through the smallest blood vessels, i.e., the capillaries [49], [50]. The microbubbles do not exhibit extravasation, hence they can be regarded as blood-pool markers. These features make DCE-US very attractive for microvascular imaging. Currently, several commercially available UCAs are approved for clinical use in different countries [50], [51]. The nontoxicity and clinical safety of these agents is today well established [50], [52], as it has also been demonstrated through several retrospective studies [26], [53], [54].

When a microbubble interacts with the US beam, it resonates at a specific frequency that is dependent on its diameter. The resonant frequency of bubbles with diameter of 1–7 μm is typically within the frequency range used in US clinical applications (1–10 MHz) [46], [55]. Oscillations of a single noncoated bubble subjected to a varying acoustic pressure are described by the Rayleigh–Plesset equation, later modified to take into account the effect of viscosity, obtaining a formulation referred to as RPNNP equation (Rayleigh, Plesset, Noltingk, Neppiras, Poritsky) [56]. This model shows that bubble oscillation is nonlinear, with asymmetric expansion and compression fronts that lead to the formation of US waves at multiples of the fundamental frequency [46], [57]. However, in the small driving pressure amplitude regime, the bubble behaves as a forced damped linear oscillator [56]. The radial motion of free bubbles can also be characterized in terms of variations in the liquid enthalpy, as described by the Gilmore equation [58], [59].

During the years, the limited applicability of the model have been expanded, relaxing assumptions, introducing additional terms or considering other models. A recent development made by Marmottant *et al.* [57] describes the dynamics of coated bubbles at insonating pressures ranging from small amplitudes, at which the bubbles show a linear response, to increasing pressure amplitudes, which lead to an original nonlinear response with buckling effects and compression-only behavior, and ultimately to shell rupture.

When imaging in fundamental mode, the microbubbles act as echo enhancers because they are able to increase the echogenicity, that is the ability to reflect an US wave, compared to that of blood and adjacent tissues [60]. However, the intensity of the reflected acoustic wave can be comparable to that of surrounding tissue, especially in hyperechoic regions and in small blood vessels, where the bubble concentration is low [47]. Consequently, fundamental imaging does not always show sufficient sensitivity to provide a good contrast-to-tissue signal ratio, and thus several contrast-specific imaging modalities have been developed, exploiting UCA characteristic properties and nonlinear behavior [47]. These include harmonic and sub-harmonic imaging, harmonic power Doppler imaging, pulse-inversion imaging, and multipulse release imaging. A complete overview of the US imaging modality is beyond the purpose of this review. More detailed information can be found in [47], [48], and [61].

During a DCE-US exam, the contrast agent is administered intravenously to the patient, either by constant infusion or as a bolus, and the time evolution of the backscattered acoustic intensity during the passage of the microbubbles in a region of interest (ROI) is acquired by an US sound transducer. The radiofrequency (RF) signal is then demodulated, compressed, and stored in quantized gray-scale or color-coded videos [62], [63]. In order to perform physiological modeling and estimate accurate quantitative hemodynamic parameters, the problem of assessing the relation between the video signal enhancement and bubble concentration arises. This problem is known as calibration and can be approached in two steps: first assessing the relationship between the UCA concentration and the backscattered acoustic intensity, and, then, studying how the latter is converted into video intensity values.

The response of the UCA to a driving acoustic pressure is mainly dependent on the backscatter coefficient, defined as the scattering cross section per unit volume, and the attenuation coefficient. If bubble oscillations are described using the Rayleigh–Plesset equation [56], assuming low driving pressures (low MI) and neglecting interaction forces between bubbles (low contrast concentration), the backscatter coefficient β is a linear function of the UCA concentration, and the backscattered acoustic intensity I is described by [62]

$$I = \frac{dV}{z^2}\beta(f)I_0 = \frac{dV}{z^2}\frac{\rho_n \sum_{\text{tot}}(f)}{4\pi}I_0 \tag{1}$$

where I_0 is the acoustic intensity insonating the UCA, dV is the volume of insonated contrast, z is the distance between dV and the transducer, ρ_n is the number of bubbles per unit volume, and $\sum_{\text{tot}}$ is the total scattering cross section. Another aspect to consider is that the presence of the contrast itself causes additional attenuation of the backscattered acoustic intensity. The attenuation coefficient is related to three main factors: microbubble decay (which can be neglected for encapsulated shells), diffusion or scattering of the acoustic energy in multiple direction, and viscous and thermal damping of the US waves. However, for low UCA concentrations, attenuation effects can be neglected and the backscattered acoustic intensity can be assumed to be linearly proportional to UCA concentration as stated by (1) [62].

Unfortunately, due to the unknown microbubble size distribution, the backscatter coefficient is usually unknown; therefore for absolute quantification a calibration procedure is needed. However, linearization of the signal is still possible, provided that all the steps in the acquisition chain from the received acoustic intensity to the US scanner output are carefully considered. The first step is the electromechanical conversion (assumed linear in the range of interest) from acoustic pressure to electrical voltage by the US transducer. This provides the raw RF voltage signal, which is then demodulated and converted into a quantized signal typically employing a logarithmic-like compression [62], [63]. Also, gamma compensation for the nonlinear relation between luminance and input voltage, as well as gain and time-gain compensations are usually performed. By considering all the steps in the conversion path, Rognin *et al.* [63] obtained a formula to relate the quantized gray level QL to the amplitude V of the raw RF signal

$$\text{QL}(V) = \text{uint8}\left[(2^8-1)\frac{20\text{dB}}{\text{LC}_{\text{DR}}}\log_{10}\left(\frac{V}{V_{\max}}10^{\frac{\text{LC}_{\text{DR}}}{20\text{dB}}}\right)\right] \tag{2}$$

where $V_{\max}$ is the maximum amplitude of the raw RF data, LC_{DR} is the dynamic range log-compression, expressed in dB, and uint8 represents the unsigned 8-bit integer quantization typecast operator. Inversion of (2) provides the amplitude V, whose squared value is linearly related to the UCA concentration by (1).

If the back conversion is done properly, Rognin *et al.* [63] showed that is possible to obtain quantitative parameter estimates from video output data as accurately as with raw RF data, provided that adequate values for system gain and dynamic range of log-compression are chosen.

2) Quantitative Modeling in DCE-US: Under the hypothesis that the increased microvascular density (MVD) associated with tumor angiogenesis translates into increased blood supply demands, many investigators have relied on tissue perfusion quantification as a potential biomarker for tumor angiogenesis [7], [15], [24], [64]–[68].

The peculiar features of the adopted contrast agent make DCE-US well-suited for perfusion quantification at both the macro and microcirculation levels. Thanks to their size, comparable to that of red blood cells, microbubbles can pass through the entire circulation with no leakage into the tissue (intravascular). Moreover, with the introduction of new contrast-specific imaging techniques, DCE-US is able to selectively enhance the microvasculature with unpaired spatial and temporal resolution [7], [46], [69]–[73]. Perfusion quantification with DCE-US has been investigated with both bolus injection [68], [70], [74] and constant infusion protocols [68], [70], [75]–[77].

After a bolus administration of an indicator substance in the circulatory system, the indicator particles travel through the different paths of the circulatory tree and reach a detection site at different times. The IDC, obtained by measuring the concentration $c(t)$ of the indicator at the detection point over time, can thus be interpreted as a probability distribution of the particle transit time through the circulatory system [see Fig. 1(a)]. According to the indicator dilution theory, given the dose M of indicator injected, the blood flow F and volume V between the injection and detection points can be calculated through Stewart–Hamilton equations as [78]

$$F = \frac{M}{\int_0^\infty c(t)dt} = \frac{M}{\text{AUC}} \tag{3}$$

$$V = F \cdot \frac{\int_0^\infty tc(t)dt}{\int_0^\infty c(t)dt} = F \cdot \text{MTT} \tag{4}$$

where AUC is the area under the IDC, and MTT is mean transit time of the indicator particles through the circulatory system.

Indicator dilution theory can be applied to DCE-US derived IDCs to provide estimates of blood flow and volume in an ROI. However, the estimates obtained will be valid only in a relative sense for two main reasons. First, the mass conservation principle, which is a basic assumption of the indicator theory, cannot be respected in practice because only a portion of the injected dose of microbubbles will actually reach the investigated ROI [65], [68]. Second, in DCE-US, the backscattered acoustic intensity rather than the contrast concentration is measured. However, at the microbubble concentration typically used for bolus injection in clinical practice, the backscattered acoustic intensity and the bubble concentration are linearly related, as experimentally demonstrated [62], [79], [80]. As a result, (3) and (4) are still valid in a relative sense, provided that the remaining underlying assumptions of indicator-dilution theory are met [68], [78], [81]. For a single-input single-output flow system, these assumptions are represented by system stationarity, constant volume and flow, instantaneous contrast injection, equivalency of indicator flow to fluid flow, and absence of recirculation.

In DCE-US, the last assumption is usually not met because the second pass of the indicator hides the down slope of the

TABLE II
SUMMARY OF THE MAIN MATHEMATICAL MODELS AVAILABLE FOR IDC FITTING OF DCE-US DATA

Model	Equation		Estimate of MTT
Lognormal	$C(\hat{t}) = \frac{\mathrm{AUC}}{\sqrt{2\pi}\sigma\hat{t}} e^{\frac{(\ln(\hat{t})-\mu)^2}{2\sigma^2}}$	(5)	$\mathrm{MTT} = e^{\mu+\frac{\sigma^2}{2}}$
Gamma variate	$C(\hat{t}) = \frac{\mathrm{AUC}}{\beta^{(\alpha+1)}\Gamma(\alpha+1)} \hat{t}^{\alpha} e^{\frac{\hat{t}}{\beta}}$	(6)	$\mathrm{MTT} = \beta(\alpha+1)$
LDRW	$C(\hat{t}) = \mathrm{AUC}\frac{e^{\lambda}}{\mu}\sqrt{\frac{\lambda\mu}{2\pi\hat{t}}} e^{-\frac{\lambda}{2}\left(\frac{\hat{t}}{\mu}+\frac{\mu}{\hat{t}}\right)}$	(7)	$\mathrm{MTT} = \mu$
FTP	$C(\hat{t}) = \mathrm{AUC}\frac{e^{\lambda}}{\mu}\sqrt{\frac{\lambda\mu}{2\pi\hat{t}^3}} e^{-\frac{\lambda}{2}\left(\frac{\hat{t}}{\mu}+\frac{\mu}{\hat{t}}\right)}$	(8)	$\mathrm{MTT} = \mu$
Lagged normal (first-order)	$C(\hat{t}) = \frac{\mathrm{AUC}}{2} K[1+\mathrm{erf}(L)]$, $\begin{cases} K = \lambda \exp\left(-\lambda t + \lambda\mu + \frac{1}{2}\lambda^2\sigma^2\right) \\ L = \frac{t-\mu-\lambda\sigma^2}{(2\sigma^2)^{1/2}} \end{cases}$	(9)	$\mathrm{MTT} = \mu + \frac{1}{\lambda}$

1) $\hat{t} = t - t_0$, where t_0 is the time delay needed for the contrast to reach the ROI
2) $\Gamma(\alpha+1) = \int_0^{\infty} x^{\alpha} e^{-x}\, dx$, gamma operator
3) $\mu, \sigma, \alpha, \beta, \gamma$, model-dependent parameters
4) erf(), error function

IDC. In addition, DCE-US curves are affected by several noise sources such as speckle noise, backscattered intensity oscillations, acoustic reverberation, and poor contrast mixing [see Fig. 1(b)]. As a result, the direct calculation of parameters such as AUC and MTT from the measured IDC is not reliable.

To overcome these problems, IDCs are usually fitted to a mathematical model that filters out the effects of noise and isolates the first pass of the indicator. In this way, hemodynamic parameters such as AUC and MTT can be calculated from the mathematical model instead of the raw data, leading to more reliable estimates of blood flow and volume. The models that are most often used to fit IDCs for DEC-US perfusion quantification after a bolus injection are listed in Table II [68]. In a data-driven modeling approach, model selection is performed on the basis of the fitting quality only, without accounting for the local physiological processes generating the data. In a system-driven modeling approach, the mathematical functions listed in Table II can be obtained by describing the system between the injection and detection sites as a physiological model.

The lognormal function [see Table II, (5)] is the probability distribution of a random variable whose logarithm is normally distributed with mean μ and standard deviation σ. It is the result of the product of a large number of independent random variables, and it has been extensively used to fit DCE-US curves [68], [82]. The connection between organ perfusion and the lognormal distribution has been investigated by Qian and Bassingthwaighte [83], who studied the distribution of flow in a network of dichotomous branching vessels. They showed that the asymmetric branching and random variation at each bifurcating point lead to an asymptotic lognormal distribution of flow. Their work, together with the demonstration by Arditi and Frinking [75] that the IDC can be expressed equivalently as transit time probability distribution or as a flow probability distribution, can be regarded as a physiological justification for the extensive use of the lognormal distribution for IDC fitting.

The gamma-variate function [see Table II, (6)] is governed by the parameters α and β, and it has been shown to fit IDCs with very good agreement [84]. As the parameter α increases, the curve becomes more skewed, while an increase in β leads to an increase of the up-slope and down-slope rates. A physiological explanation for the function parameters has been emphasized by Davenport [85] and by Mischi [86], who described the flow in a blood vessel as a distributed model consisting of a cascade of mixing chambers. Considering a number n of mixing compartments of equal volume V and flow rate Q, Davenport showed that the concentration in the nth compartment behaves as a gamma-variate function with parameters $\alpha = n-1$, accounting for the theoretical number of mixing chamber, and β being the time constant of the compartments, and given by the ratio of theoretical volume over the flow rate. A physiological interpretation of the gamma-variate function for IDC fitting can also be found by modeling the bolus kinetic as a convective-dispersive transport process. In its most general form, the transport of an indicator in a single vessel can be described as [87]

$$\frac{\partial c(\mathbf{p},t)}{\partial t}\nabla J(\mathbf{p},t) + R(\mathbf{p},t) = -\nabla\left[v(\mathbf{p},t)c(\mathbf{p},t) - D(\mathbf{p})\nabla c(\mathbf{p},t)\right] + R(\mathbf{p},t) \quad (10)$$

where $c(p,t)$ is the concentration of the indicator at time t and position $p(x,y,x)$, $R(p,t)$ is the net rate of production of the indicator, $J(p,t)$ is the total flux of the indicator, which is equal to the sum of a convective term and a diffusion term, $v(p)$ is the indicator velocity, and $D(p)$ is the indicator diffusion coefficient. In general, diffusion is due to the Brownian motion of the contrast molecules driven by heat and concentration gradients. This phenomenon is often referred to as molecular diffusion. However, in the presence of convection through a microvascular network, diffusion is mainly determined by fluid-dynamic effects, such as flow profile in larger vessels and the multipath trajectories across the microvascular bed. The combined action of convection and molecular diffusion was addressed by Taylor [88] as apparent dispersion.

Setting $R(p,t)$ equal to zero, and simplifying (10) in one dimension (discarding the effects of radial diffusion), lead to the monodimensional diffusion with drift equation, which describes

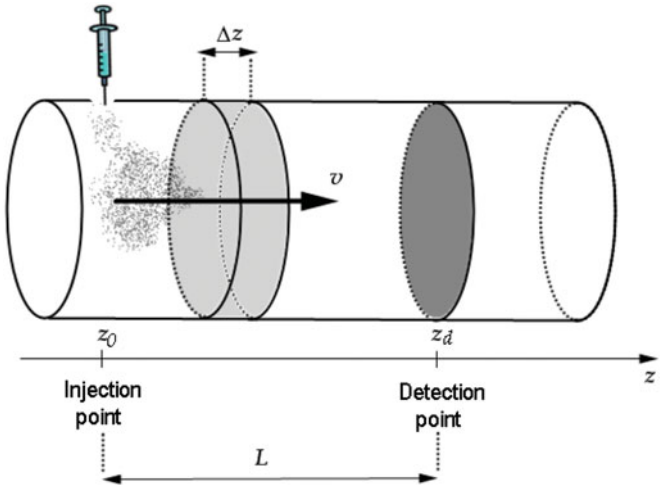

Fig. 2. Schematic of a vessel modeled as an infinite-long tube. A bolus of contrast agent is injected upstream at $z = z_0$ and the concentration of the contrast agent over time is measured downstream at $z = z_d$.

the indicator transport as a dispersion process superimposed on a linear drift

$$\frac{\partial c(z,t)}{\partial t} = \frac{\partial}{\partial z}\left(D\frac{\partial c(z,t)}{\partial z}\right) - v\frac{\partial c(z,t)}{\partial z}. \tag{11}$$

Harpen and Lecklitner [89] obtained (11) for a vessel of cross-sectional area A and flow rate Q, by spatially averaging the rate of change of $c(z,t)$ over a vessel characteristic length z, and expanding $C(z-\Delta z,t)$ into a Taylor series about z (see Fig. 2). They solved the resulting equation for the fast injection of an indicator at $z,t=0$, assuming an average velocity $v = Q/A$, and the dispersion coefficient ($D = \Delta z Q/2A$) to be independent of the position along the vessel, and resulting from a number of factors including longitudinal diffusion, radial diffusion in the presence of laminar flow, and turbulence. The solution is a gamma-variate of the form

$$C(t) = \text{const} \cdot t^a e^{-\frac{t}{\beta}} \tag{12}$$

with parameters $\alpha = \Delta z v/4D$, and $\beta = 4D/v^2$.

The local density random walk (LDRW) model [see Table II, (7)] and the first time passage (FTP) model [see Table II, (8)] are also possible solutions of the diffusion with the drift equation [(11)]. Because of their excellent fit and physiological interpretation, they have been extensively used to model DCE-US derived IDCs [68], [84], [90]–[94]. They describe the injection of an indicator into a straight infinitely-long tube of cross-sectional area *A*, where a fluid flows with a constant velocity v (see Fig. 2). The LDRW solution was first introduced by Sheppard and Savage [95] using a stochastic approach. They assumed a random walk of the indicator particles due to Brownian motion, which interact only by elastic collisions. Due to the random walk hypothesis, each step is independent from the previous one, and the transport of the indicator particles can be regarded as a Wiener process [96]. The boundary conditions are represented by an initial concentration at the injection point which is represented by a delta function of amplitude equal to the injected dose M divided by the area A (fast injection), and by the mass conservation principle. Equivalent formulations of the LDRW equation were found by Norwich and Zelin [93] and by Wise [97]. The former solved (12) with no particular boundary conditions at the outlet, and obtained a Gaussian distribution that translates in space at fluid velocity, and whose variance increases linearly in time, as expressed by

$$C(z,t) = \frac{M}{\sqrt{4\pi D A^2 t}} e^{-\frac{(z-vt)^2}{4Dt}}. \tag{13}$$

Wise [97] used a random walk approach to obtain a model governed by the parameters μ which represents the MTT, and λ which is responsible for the skeweness of the curve [see Table II, (7)]. Bogaard *et al.* [90] underlined the analogy between these two formulations, by setting AUC $= m/vA$ and $\lambda = vL/2D$, where L represents the distance between detection and injection points. They also emphasized the relationship of the skeweness parameter λ with the Peclet number (Pe), which is a dimensionless number that relates the relative contributions of convection and diffusion in a dilution process. This relationship is given by $Pe = 2\lambda = \mu L/D$, and suggests that for high diffusion values the resulting curve is more symmetric and less skewed. The only difference between the FTP and the LDRW models resides in the boundary condition at the outlet. The FTP model [see Table II, (8)] assumes the presence of a virtual absorbing barrier at the outlet, so that a microbubble traversing the detection site is immediately destroyed, while the LDRW model allows for multiple passages of the indicator through the detection site. As a consequence, in the FTP model, as in every model in which multiple passages are not contemplated, the MTT is equivalent to the mean residence time (MRT), and both equal to μ. Differently, in the LDRW model the MRT is longer than the MTT and given by $\mu(1+1/\lambda)$. Therefore, the MRT exceeds the MTT by a quantity $\mu/\lambda = 2D/v^2$, suggesting that large diffusion constants lead to multiple passages through the detection site [74].

The lagged normal function was first proposed by Bassingthwaighte *et al.* [98] to model the transport of blood from a larger artery into a microvascular bed. In general, the large artery is modeled as a Gaussian function representing the dispersion of the indicator transit times, and the microvascular bed as a series of well-mixed compartments, described by exponential functions. The resulting function is thus obtained as a convolution between a Gaussian density function with a number of exponentials, defined by the order of the lagged-normal [99]. For the first-order lagged normal function [see Table II, (9)], the MTT is given by $\mu + 1/\lambda$, which is the sum of MTTs of the Gaussian and exponential functions, respectively.

Alternative to the bolus injection, perfusion quantification with DCE-US can be accomplished with a constant infusion protocol, by applying the destruction-replenishment technique. According to this method, a high MI pulse is used to destroy the microbubbles within an ROI, and the subsequent replenishment by inflowing microbubbles is observed in real time at low MI (see Fig. 3). Fitting the replenishment kinetic to a proper mathematical model allows estimating blood volume and mean blood velocity within the ROI, from which blood flow can be calculated. The replenishment curve can also be obtained by intermittent imaging using multiple high MI bursts, whereby the

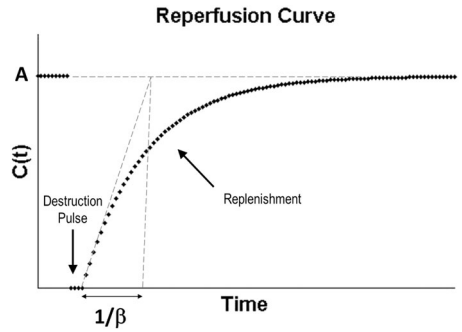

Fig. 3. Reperfusion curve: after the application of an high pressure pulse, which destroys all the microbubble whithin the ROI $(C(t) = 0)$, the microbubbles refill the ROI, and the concentration rises monotonically until the replenishment plateau is reached.

frame rate of the US scanner is varied to sample the reperfusion curve at different time instants [100].

Wei *et al.* [77] were the first to apply the destruction-replenishment method for quantification of myocardial blood flow. They fitted the replenishment curve to a model represented by a monoexponential function of the form

$$y = A\left(1 - e^{-\beta t}\right) \tag{14}$$

and related the parameter A to the blood volume, and β to the blood velocity [58]. Blood flow is then represented by their product. The model is simple and straightforward, and it has been extensively used for perfusion measurements with the destruction-replenishment technique [67], [101]. However, the model does not consider the US beam diffraction properties in the ROI, and thus it is operator and equipment dependent. In response, many authors have proposed alternative models to take into account vascular morphology and beam characteristics. Krix *et al.* [100] pointed out the existence of multiple vessels with different flow rates and entry angles within the imaging plane, and proposed a piece-wise model that separates a linear and a nonlinear component. To explain the sigmoidal rather than monoexponential shape of the refill curve, Lucidarme *et al.* [102] highlighted the importance of the width of the destruction zone that is generally larger than the observed ROI, causing a delay in the replenishment due to the destruction of microbubbles in the feeding vessels. As explained by Potdevin *et al.* [103], beside the difference between the destruction-zone and read-out zone, which changes within the beam elevation plane, and the distribution of velocities within the ROI, the replenishment curve is also influenced by the US beam point spread function. Recognizing all these factors, Arditi and Frinking [75] proposed a formalism that describes the replenishment function $S(t)$ in a single vessels as

$$S(t) = A\,\mathrm{perf}\left[1.94\frac{KT}{2\tau}(t-\tau)\right] \tag{15}$$

where A represents the estimated blood volume, K is the transmit-receiver parameter, T is the width of the destruction zone, τ is the time needed to replenish half of the bubble destruction zone, and $\mathrm{perf}(q) = 0.5(1 + \mathrm{erf}(q))$, where erf is the error function. The extension to multiple flow values is obtained by averaging the replenishment function of a single vessel, over the distribution of transit times $PD(\tau)$ resulting from a vascular tree

$$S(t) = A\int_0^\infty PD(\tau)\mathrm{perf}\left[1.94\frac{KT}{2\tau}(t-\tau)\right]d\tau. \tag{16}$$

They considered the use of a lognormal probability density function of transit times as the most indicated in many physiological tissues, but they also suggested that perfusion in some tissues may be better represented by other distributions, e.g., referring to the ones shown in Table II.

An alternative model was proposed by Hudson *et al.* [76], who separated the effects of the US beam parameters from the flow specific parameters, representing the replenishment function as a flow function $F(x, y, z, t)$ weighted by a beam function $B(x, y, z)$ over the imaging volume as

$$S(t) = \int_V B(x,y,z)F(x,y,z,t)dV. \tag{17}$$

To calculate the flow function in a vascular network, they suggested that a group of multiple vessels with different flow rates can be represented by a single vessel that has a cross-sectional area A equal to the sum of the single vessel areas, and a unique velocity profile v obtained by weighting the individual vessel velocities. Based on the above-mentioned model by Qian and Bassingthwaighte [83], they assume this velocity profile to be lognormally distributed and expressed the flow function as

$$F(z,t) = \frac{A}{2}\mathrm{erf}\left(\frac{\ln(v) - \mu_f}{\sigma_f\sqrt{2}}\right) \tag{18}$$

where μ_f and σ_f are the mean and standard deviation of the variable $\ln(v)$, respectively. To account for the difference between the destruction and imaging zones, and for the depth-dependent US beam pressure in the imaging plane, they expressed the beam function as

$$B(y,z) = \mathrm{sinc}^2\left(\frac{2z}{\mathrm{BW}(y)} - \frac{2\mathrm{BS}(y) + \mathrm{BW}(y)}{\mathrm{BW}(y)}\right)\prod(y,z) \tag{19}$$

where $\mathrm{BW}(y)$ is the field elevation beam profile, $\mathrm{BS}(y)$ accounts for the separation zone between the detection and disruption boundaries, and $\prod(y,z)$, is a band-pass filter that truncates the main lobe of the sinc^2 function. In addition, they proposed a possible method to separate the contribution to the total flow of small and large blood vessels, based on the observation that the early part of the replenishment is mainly dominated by large vessels and fast flow velocities, while smaller vessels mainly contribute later in time [104].

Although many models and protocols for perfusion quantification at the macro and microvascular level are available, the complexity and heterogeneity of the angiogenic tumor vasculature raises some doubts on the reliability of perfusion to characterize tumor angiogenesis. High perfusion could result from the lack of vasomotor control and from the presence of arterio-venous shunts, but, on the other hand, the tortuosity, irregularity, and increased interstitial pressure could lead to a decreased blood flow [3], [13], [14]. Moreover, tumor vascularity is often heterogeneous with a usually low-perfused necrotic

center surrounded by a highly perfused periphery [15], [69]; it has also been shown that the percentage of perfused vessels in a tumor can vary between 20% and 85% [105]. These observations are supported by the work of Karshafian *et al.* [106] and Kuenen *et al.* [79]. The former developed two fractal vascular models, one representing the kidney normal vasculature, and the other representing the tumor-like chaotic vasculature. These models are generated through a fractal branching algorithm, in which the degree of disorder can be controlled by changing the permissible variability range of the branching parameters. Interestingly, the simulation of the tracer kinetic in the two vascular models, under the same condition of flow and volume, showed reperfusion curves with same initial slope and plateau, corresponding to the same flow and volume estimates, but different curve shapes, with a slower rise in the case of the tumor-like vascular model. Accordingly, the shape of transit time distributions was also different, with a much wider distribution in the tumor-like case. Their work demonstrated that perfusion quantification is not able to recognize differences in the tracer kinetic resulting from different vascular architectures, and, although without providing a specific method, suggested that the vascular morphology could be assessed based on the shape of the transit-time distribution curve.

Although with different results, Kuenen *et al.* [79] also suggested that perfusion may not be able to characterize changes in the microvasculature, which may be better reflected by dispersion characteristics. In response, they developed a novel method for the assessment of the microvasculature architecture, based on the analysis of the dispersion kinetic of an indicator bolus. The method is based on the modified local LDRW (mLDRW), which is a solution of the convective-dispersion equation [(11)]. This solution is obtained from the classic LDRW considering a short segment Δz of the infinitely long tube (see Fig. 2) and replacing the initial boundary condition of fast bolus injection with a local boundary condition. Specifically, the assumptions are that 1) the spatial contrast concentration at time t_1 just before the passage at the detection site z_d is Gaussian distributed with mean $z_1 = z_d - \Delta z$, and variance $\sigma(t_1)$; 2) the hemodynamic parameters are locally constant, i.e., $D(z) = D_l$ and $v(z) = v_l$ for $z_1 - \Delta z \leq z \leq z_d$. By making these assumptions and with a different parameterization, the dilution process is characterized locally at a specific detection site as

$$C(t) = \mathrm{AUC}\sqrt{\frac{\kappa}{2\pi(t)}}e^{-\frac{\kappa}{2t}(t-\mu)^2}. \tag{20}$$

The new parameterization defines a local dispersion-related parameter κ, which is given by $\kappa = \lambda/\mu = v_l^2/2D_l$, and that can be interpreted as the local ratio between convective time and squared dispersion time. As shown in Fig. 4, high local dispersion, hence low values of κ, results in wider spreading of the IDC, while low values of local dispersion, which may be expected in irregular and tortuous angiogenic vessels, yield a more symmetric curve. Differently from the LDRW, this new model gives a characterization of the shape of the IDC at a specific detection site independent of bolus history and of the distance between injection and detection points, which in practice are not known. The local degree of dispersion can also be characterized with a full spatio-temporal approach, by looking at the shape similarity of neighboring IDCs [13], [107].

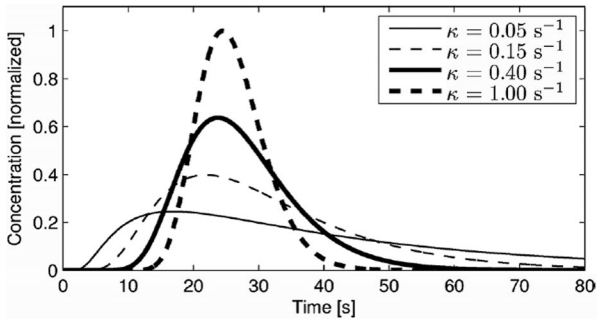

Fig. 4. IDC obtained by simulating the mLDRW model for different values of κ, and $\mu = 25$ s. Taken from [79].

To summarize, several models for the assessment of tumor angiogenesis with DCE-US have been developed. Angiogenesis has been addressed by estimating perfusion-related parameters from mathematical models describing the indicator dilution process, for both UCA bolus injection and constant infusion protocols. Alternatively, angiogenesis can be characterized by other hemodynamic parameters, e.g., dispersion, which take into account the influence of the vasculature architecture on the dilution process.

B. Extravascular Contrast Agents: MRI and CT

1) Contrast Agent Properties and Signal Calibration:

a) DCE-CT: In CT imaging, the signal is given by the differences in attenuation coefficients that various tissues exhibit. After image reconstruction, each pixel gives CT density defined as [44]:

$$CT = 1000\frac{\mu_T - \mu_{H_2O}}{\mu_{H_2O}} \tag{21}$$

where CT is measured in Hounsfield, and μ_T and μ_{H_2O} are the linear attenuation coefficients of tissue and water, respectively. Current DCE-CT contrast media are obtained from a triiodinated benzene ring and differ for their chemical and physical properties, including chemical structures, osmolarity, iodine content, and ionization solution. The first to be introduced were the high osmolarity ionic contrast media, which have a ratio 1.5 ionic compound with a sodium concentration similar to blood and a pH between 6 and 7. In order to reduce the hypertonicity side effects, ratio 3 low-osmolarity ionic and nonionic contrast media were later introduced, and more recently, a new class of isomolar contrast medium (ratio 6 nonionic dimmer) became available on the market [108]. Due to their lower toxicity and lower incidence of adverse side effects, the most commonly used CT contrast agents are nonionic low-osmolar iodinated agents [28]. Following intravenous injection, the contrast agent distributes between the vascular and the extravascular spaces. There is a negligible intracellular uptake, and excretion is via glomerular filtration [8]. Because of their high atomic number, the contrast media act as radio-opaque elements, causing

CT X-ray beam absorption and, thus increasing the total attenuation coefficient. After administration, the total attenuation coefficient of a voxel is dependent on the tracer concentration as follows [44]:

$$\mu_T = \mu_{T,0} + \mu_{CA}(t) = \mu_{T,0} + kC(t) \tag{22}$$

where $\mu_{T,0}$ is the tissue attenuation coefficient before tracer administration and $\mu_{CA}(t)$ is the contribution to the attenuation coefficient due to the presence of the contrast medium, which is directly proportional to the concentration of the tracer in the tissue. Thus, the conversion from signal intensity to tissue tracer concentration is straightforward, and can be derived as

$$CT_T(t) - CT_0 = kC(t). \tag{23}$$

b) DCE-MRI: DCE-MRI signal conversion is more complicated as several phenomena contribute to the acquired signal. In general, contrast in MR images depends on proton spin density, and on longitudinal (T1) and transverse (T2 and T2*) relaxation times [44], [109]. MRI contrast agents can be either paramagnetic, superparamagnetic, or ferromagnetic, and generally act by changing the relaxation times of water protons through the interaction with the outer shell electrons of the magnetic compound within the tracer. The ability to shorten T1 and T2 relaxation times is described by the relaxivities R1 and R2, respectively. The ratio between R1 and R2 distinguishes between positive contrast agents, which have a high R1 and low R2 and, hence, produce positive enhancement in T1-weighted images, and negative contrast agents, which have a larger R2 and produce negative enhancement on T2-weighted images [109], [110]. The most commonly used MRI contrast media in radiology are positive paramagnetic agents, made of small molecular weight compounds that distribute nonspecifically in the blood plasma and extravascular extracellular space of the body after administration. The metal ion Gd3+ exhibits interesting magnetic properties, represented by seven unpaired electrons in the outer shell and a slow electronic relaxation time. The toxicity of this heavy metal can be reduced by combining it with chelating molecules to increase the hidrophilicity, leading to a rapid excretion through the kidneys with an elimination half life of about 15–120 min [27], [111]. These properties make gadolinium chelates the preferred contrast agents for MRI. The first CA approved for clinical MRI applications in humans was the anionic gadolinium diethylenetriaminepentaacetate complex, Gd-DTPA, which is now routinely used for contrast MRI in clinical practice [10], [28].

When a gadolinium-based MRI contrast agent is injected into a vein, the short distance dipole–dipole interactions cause a decrease in the T1 relaxation rate, which results in signal enhancement in T1-weighted images. At the same time, the susceptibility-induced gradients surrounding the contrast agent cause a signal dephasing that leads to a T2* shortening, resulting in signal loss [111]. Depending on whether a T1-weighted or a T2*-weighted sequence is employed, the two most routinely used clinical approaches in DCE-MRI are referred to as relaxivity based or susceptibility based, respectively [2]. Both techniques measure the influence that the same contrast agent has on the relaxation times. However, the two methods are based on inherently different effects and they are therefore able to highlight hemodynamic features at different levels.

T2*-shortening is a long-range effect that may extend several millimeters beyond the physical effect of the contrast agent [2], [112]. Moreover, it dominates in areas where the contrast agent is retained within the vasculature because of the increased induced gradients resulting from compartmentalization. These effects make T2*-weighting more sensitive to large blood vessels and prone to errors in case of marked capillary leakage [2], [112], [113]. As a result, the susceptibility based method, also known as dynamic susceptibility contrast MRI, is mostly used to measure organ-level hemodynamic features in tissues where the contrast agent remains intravascular. One common application is the assessment of perfusion and blood volume in the brain, where intact blood-brain barriers (BBB) prevent the agent from leaking into the brain tissue [2], [7].

Conversely, if the contrast agent leaks into the extravascular space, due to a more homogeneous distribution of the contrast, the susceptibility induced gradients are reduced and the short-range relaxivity effects become more dominant [2], [114]. T1-weighted imaging is very sensitive to the low concentrations of Gd-DTPA that permeate through capillary walls and it is thus preferred for imaging features of tumor angiogenesis such as permeability and leakage space [44]. For the above reasons, this paper focuses on Gd-DTPA based T1-weighted DCE-MRI.

At tracer concentrations routinely used in clinical practice (0.1–0.2 mmol/kg body weight) a linear relationship between T1 shortening and tracer tissue concentration can be derived as follows [109], [114]:

$$\frac{1}{T_1} = \frac{1}{T_{10}} + r_1 C_T \tag{24}$$

where T_1 and T_{10} are the longitudinal relaxation times before and after contrast injection, respectively, r_1 is the contrast spin-lattice relaxivity constant, and C_T is the tissue tracer concentration. To acquire the T1-weighted images, spoiled gradient echo sequences (FLASH) are typically used [10], [112], [115], [116]. The resulting signal intensity is described as

$$S = G\frac{\sin\alpha\,(1-\exp(-\mathrm{TR}/T_1))}{(1-\cos\alpha\,\exp(-\mathrm{TR}/T_1))}\exp(-\mathrm{TE}/T2^*) \tag{25}$$

where α is the flip angle, TR is the repetition time, TE is the echo-time, and G is a constant which depends on proton density, and machine settings. Equation (25) shows the dependency on T2* relaxation time. By using sequences with very short TE, the influence of T2* changes on the total signal intensity becomes negligible [44], [111], [114], [116], [117], while the most commonly used strategy to overcome the dependence on machine settings is to relate the signal intensity postcontrast to the signal intensity precontrast, so as to obtain [114], [118]

$$\frac{S_{Gd}(t) - S_0}{S_0} \approx r_1 T_{10} C_T(t) \tag{26}$$

where S_0 and S_{Gd} are the signal intensities before and after contrast injection, respectively. Equation (25) provides the conversion from signal intensity to contrast concentration, provided that the contrast spin-lattice relaxivity constant (r_1) is known, and the tissue longitudinal relaxation time T_{10} before contrast

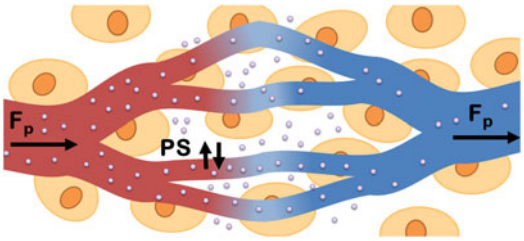

Fig. 5. Schematic of the vascular-interstitial contrast agent exchange. The contrast agent is carried by the blood plasma with flow F_p and it exchanges with the interstitium at a rate PS. Finally, it is reabsorbed in the capillaries at the same rate PS and cleared out by venous circulation.

injection has been measured. The appropriate r_1 value for each specific contrast agent and magnetic field strength can be found in the literature [119], while the native tissue T_{10} can be measured with a dedicated MRI sequence (e.g., saturation recovery, inversion recovery, spoiled gradient echo) [120], [121] prior to the acquisition of the dynamic series.

Since the kinetic behavior of CT and MRI contrast agents is equivalent, once a proper conversion from signal intensity to tissue tracer concentration has been performed [(23), (26)], the analysis becomes independent of the adopted imaging modality and the same mathematical models are typically applied to the obtained concentration-time curves (CTCs) [44], [122].

2) Quantitative Modeling in DCE-CT and DCE-MRI:

The exchange of an extravascular extracellular contrast agents between blood plasma and tissue can be represented schematically as in Fig. 5.

The contrast agent is carried by the blood plasma from the injection site into the capillary bed, where it crosses the vascular endothelium and distributes into the interstitium. Then, it leaks back into the capillaries and it is cleared out by the venous circulation. The application of the principles of tracer-kinetic theory to such a system enables the assessment of well-defined physiological parameters related to tissue perfusion, permeability, cellularity, and vascularity. To this end, CTCs measured with DCE-MRI and DCE-CT are fitted by suitable pharmacokinetic models, able to describe the vascular-interstitium contrast exchange. This is mainly dependent on four parameters:

- The *plasma flow* F_p (ml/min/100 ml), which quantifies the volume of plasma flowing into the vessels per unit of time and of tissue volume.
- The *permeability-surface area product* PS (1/min), which quantifies the rate at which the indicator travels from the plasma to the interstitium.
- The *fractional plasma volume* $v_p = V_p/V_T$, the ratio between V_p and total tissue volume V_T.
- The *fractional extravascular volume* $v_e = V_e/V_T$, the ratio between the volume of the extravascular extracellular space V_e and the total tissue volume V_T.

From these, other commonly derived parameters are

1) the *MTT* $T(s)$, which can be derived from the central volume theorem given in (5), setting $V = v_p + v_e$ and $F = F_p$. The extracellular MTT T_e can also be derived in the same way by setting $V = v_e$. On the contrary, the estimation of the plasma MTT T_p is, in principle, not as straightforward because, due to the double inlet (arterial and trans-endothelial), the central volume theorem cannot be directly applied;
2) the *extraction fraction* E, which quantifies the percentage of indicator particles that are extracted into the tissue, and it can be calculated from the Renkin–Crone [123] relationship as
$$E = 1 - e^{-\mathrm{PS}/F_p}; \tag{27}$$
3) the *volume transfer constant* K^{trans} (1/min), which expresses the rate at which the indicator particles cross the vascular endothelium and it can be derived as the product between the plasma flow F_p and the extraction fraction E as
$$K^{\mathrm{trans}} = F_p\left(1 - e^{-\mathrm{PS}/F_p}\right). \tag{28}$$
In general, K^{trans} reflects both permeability and perfusion. However, in the boundary regime of very high flow (permeability-limited condition), K^{trans} is purely permeability weighted, while in case of very high PS (flow-limited condition), it mainly reflects the flow;
4) the rate constant between the intravascular and extravascular spaces k_{ep} (1/min), which is given by K^{trans} divided by v_e.

According to Zierler [124], in a system with a single inlet and a single outlet, in which the indicator is introduced at a peripheral site, the output $o(t)$ is given by the convolution of the input $i(t)$ with a tissue-specific response function $r(t)$, represented by the probability density of transit times through the system, as
$$o(t) = i(t) * r(t). \tag{29}$$
In this context, typical inputs and outputs are represented by masses, concentrations, and flows. Based on this, the mass $M_t(t)$ of indicator which is still in the system at time t can be calculated as the convolution of the input curve (arterial plasma concentration $C_a(t)$ multiplied by the plasma flow F_p) with the tissue residue function $R(t)$ as [125]
$$M_t(t) = F_p C_a(t) * R(t) \tag{30}$$
where
$$R(t) = 1 - \int_0^t r(\tau)d\tau. \tag{31}$$
Dividing (33) by the total volume V_T, we can express it in terms of measured concentration $C_t(t)$ as
$$C_t(t) = \frac{F_p}{V_T} C_a(t) * R(t) = C_a(t) * H(t) \tag{32}$$
where $H(t)$ is the tissue impulse response function.

While $H(t)$ or $R(t)$ are typically found as analytical solutions of suitable pharmacokinetic models, the arterial concentration $C_a(t)$, commonly referred to as arterial input function (AIF), is usually estimated or measured separately. When a feeding artery is visible in the imaging plane, the AIF is measured from the DCE series, and possibly fitted by a model-based function to deal with low signal-to-noise ratio (SNR) and constrain it to a physiologically realistic input function [126]. However,

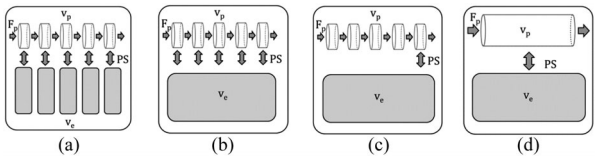

Fig. 6. Schematics of (a) DP model, (b) TH model, (c) AATH model, and (d) 2CXM model.

a suitable artery is not always present in the imaging plane. Moreover, the temporal resolution may be too low to capture the fast AIF dynamics, and saturation problems can arise due to the high contrast concentration in the feeding artery. In these cases, possible remedies are to use an analytical form of the AIF from the literature [118], [127], or to use a population averaged AIF [128]–[130].

In the following, several mathematical models commonly used to describe the vascular-interstitium contrast exchange are presented. They differ in the way in which the two exchanging regions are represented, in the assumptions and approximations made, and in the parameters that they are able to estimate. Based on the wider applications they have found, in this review, we limit the discussion to those models which assume that 1) the interstitium exchanges only with the blood plasma (no lymphatic drainage is considered), 2) the capillary permeability is the same in both directions, and 3) the diffusion of the contrast agent within the interstitium is negligible.

In general, the total concentration in a voxel of tissue can be described as a weighted sum of the intravascular and extravascular concentration as

$$C_t(t) = v_p C_p(t) + v_e C_e(t) \tag{33}$$

where $C_p(t)$ and $C_e(t)$ are the tissue plasma and extravascular concentrations, respectively. The law of mass conservation, which states that no contrast agent is accumulated in the system, must also be satisfied

$$\frac{dC_t(t)}{dt} = F_p C_p(t) - F_p C_v(t) \tag{34}$$

where $C_v(t)$ is the venous concentration.

In the distributed parameter (DP) model [128], [131]–[133] [see Fig. 6(a)], the intravascular space is represented as a plug-flow system, which describes blood vessels as a tube of length L divided into small sectors of length dx. The position along the tube is a function of x, with arterial inlet at $x = 0$ and venous outlet at $x = L$. The flow F_p and the permeability-surface area product PS are equal in each sector, and thus, independent of x. The extravascular space is represented as a distributed system composed of infinitesimal compartments which exchange with the closest capillary at a rate PS, but do not exchange with each other [see Fig. 6(a)]. The differential equations representing this model are

$$v_p \frac{\partial C_p}{\partial t}(x,t) = -F_p L \frac{\partial C_p}{\partial x}(x,t) - \mathrm{PS} C_p(x,t) + \mathrm{PS} C_e(x,t), \tag{35}$$

$$v_e \frac{\partial C_e}{\partial t}(x,t) = \mathrm{PS} C_p(x,t) - \mathrm{PS} C_e(x,t). \tag{36}$$

Solving (35) and (36) with boundary conditions $C_p(x = 0, t) = \delta(t)$, $C_p(x > 0, t = 0) = 0$, $C_e(x, t = 0) = 0$, $C_e(x = 0, t) = 0$, yields for $R(t)$

$$R(t) = R_1(t) + R_2(t - T_p) \tag{37}$$

with $R_1(t)$ representing the vascular transit phase described by

$$R_1(t) = u(t) - u(t - T_p) \tag{38}$$

and $R_2(t)$ representing the parenchyma back-flux phase described by

$$R_2(t) = u(t)\left[1 - \exp\left(-\frac{\mathrm{PS}}{F_p}\right)\right] \cdot \left[1 + \int_0^t \exp\left(-\frac{\mathrm{PS}}{v_e}\tau\right)\sqrt{\frac{\mathrm{PS}}{v_e}\cdot\frac{\mathrm{PS}}{F_p}\cdot\frac{1}{\tau}}\cdot I_1\left(2\sqrt{\frac{\mathrm{PS}}{v_e}\cdot\frac{\mathrm{PS}}{F_p}}\tau\right) d\tau\right] \tag{39}$$

where $u(t)$ represents the Heaviside unit step function, T_p the vascular transit time given by $T_p = v_p/F_p$, and I_1 the modified Bessel function.

The tissue homogeneity (TH) model [see Fig. 6(b)] was first described by Johnson and Wilson [134] and later applied for analysis of indicator transport in the brain by Sawada *et al.* [135]. In this model, the intravascular space is still represented as a plug-flow system, while the extravascular space is described as a well-mixed compartment. Equation (35) is thus modified as

$$v_e \frac{dC_e}{dt}(t) = \mathrm{PS} C_p(t) - \mathrm{PS} C_e(t). \tag{40}$$

Although model fitting can be obtained in the Laplace domain [134], the lack of an analytical solution in the time domain has limited the application of this model.

In response, Lawrence and Lee [125] developed the adiabatic approximation to TH (AATH) model [see Fig. 6(c)], which is based upon the observation that the dynamics in the intravascular space are much faster compared to those in the extravascular space, and thus the slow event can be considered constant during the fast event. Similarly to the TH model, the AATH model describes the intravascular space as a plug-flow system and the extravascular space as a well-mixed compartment, but further assumes the vascular-interstitial exchange to take place only at the venous end ($x = L$) [see Fig. 6(c)]. The resulting partial differential equation are [128]

$$v_p \frac{\partial C_p}{\partial t}(x,t) = -F_p L \frac{\partial C_p}{\partial x}(x,t) \tag{41}$$

$$v_e \frac{\partial C_e}{\partial t}(t) = \mathrm{PS} C_p(L,t) - \mathrm{PS} C_e(L,t). \tag{42}$$

The analytical solution of (41) and (42) yields for $H(t)$ [136]

$$H(t) = \begin{cases} F_p & \text{for } 0 \le t \le T_p \\ \mathrm{PS} e^{-\frac{\mathrm{PS}}{v_e}(t - T_p)} & \text{for } t \ge T_p \end{cases} \tag{43}$$

where $T_p = v_p/F_p$.

A further simplification of the intravascular space as a well-mixed compartment leads to the two-compartments exchange (2CXM) model [see Fig. 6(d)], for which mass conservation in

the plasma space and interstitium leads to

$$v_p \frac{dC_p(t)}{dt} = F_p C_a(t) - F_p C_p(t) + \mathrm{PS} C_e(t) - \mathrm{PS} C_p(t) \tag{44}$$

$$v_e \frac{dC_e(t)}{dt} = \mathrm{PS} C_p(t) - \mathrm{PS} C_e(t). \tag{45}$$

These equations were first proposed by Morales and Smith [137] and reviewed by Kety [138] in the context of blood-tissue exchange of inert gasses, and later introduced by Brix *et al.* for assessment of the microvasculature in DCE-CT [139] and DCE-MRI [140] by numeric integration of (44) and (45) with the Kutta–Merson method. An analytical solution for the impulse residue function $R(t)$ of the model is provided in [40] and [141] as

$$R(t) = A\exp(-\alpha t) + (1-A)\exp(-\beta t) \tag{46}$$

where the variables A, α, and β are related to the physiological parameters F_p, PS, v_p, and v_e by the following relationships:

$$\begin{aligned} &\frac{F_p}{v_p} = A(\alpha-\beta)+\beta; \qquad \frac{\mathrm{PS}}{v_p} = \frac{\alpha\beta}{A(\alpha-\beta)+\beta}; \\ &\frac{\mathrm{PS}}{v_e} = \alpha+\beta-\frac{\alpha\beta}{A(\alpha-\beta)+\beta}. \end{aligned} \tag{47}$$

The four-parameter models presented above are able to provide a separate estimation of F_p, PS, v_e, and v_p. However, the reliability of the estimation depends on several factors including acquisition settings (time resolution, acquisition window, SNR) [142]–[144], and tissue hemodynamic status. For instance, in boundary regimes such as weakly vascularized tissue ($v_p \approx 0$), highly vascularized tissue ($v_e \approx 0$), highly perfused tissue ($F_p \approx \infty$), negligible indicator exchange (PS ≈ 0), and fast indicator exchange (PS $\approx \infty$), some of the parameters remain undetermined [128], [133]. While the acquisition settings are known, usually no or limited *a priori* knowledge is available on the tissue hemodynamic conditions, and the reliability of the estimated parameters remains unknown.

Historically, simpler three- or two-parameter models have found widespread use in clinical practice. Although their preferred use was mostly dictated by the limitations in signal quality, and spatio-temporal resolution of the DCE acquisitions, which made the estimation of four free parameters challenging, these simpler models can be seen as particular solutions of the more general four-parameter models in one of the boundary regimes.

The model which has found the most widespread use in clinical practice is the extended Tofts model (eTM) [145], which can be derived either from the DP, TH, AATH, or 2XCM models by considering the boundary regime of highly perfused tissue, for which $F_p \approx \infty$. In this case, the solution takes the form

$$C_t(t) = v_p C_p(t) + K^{\mathrm{trans}} e^{-K^{\mathrm{trans}}/v_e\, t} * C_a(t). \tag{48}$$

This model allows for the separate estimation of K^{trans}, v_p, and v_e. Due to the infinite flow assumption, the intravascular concentration can be considered equal to the arterial concentration ($C_p(t) \equiv C_a(t)$), and K^{trans} is equivalent to PS.

The eTM is an expansion of a simpler model, independently published by Tofts and Kermode [127], Larsson *et al.* [146], and Brix *et al.* [147], which became known as Tofts model (TM), owing a consensus paper of 1999 [148]. In the TM, the further assumptions of negligible capillary contribution to the total tissue concentration is made. This is equivalent to setting $v_p = 0$ in (48), leading to

$$C_t(t) = K^{\mathrm{trans}} e^{-K^{\mathrm{trans}}/v_e\, t} * C_a(t). \tag{49}$$

Here, only K^{trans} and v_e can be estimated separately, while the estimation of v_p is no longer possible. These models have proven useful in a number of clinical applications [149]–[153]. However, care must be taken when applying the eTM and TM, especially when no prior knowledge about the tissue hemodynamic status is available [132], [143]. In fact, it was shown that the TM provides accurate estimates only for weakly vascularized tissue, while the eTM is applicable only in case of weakly vascularized or highly perfused tissue. In general, the estimated K^{trans} reflects both permeability and perfusion, unless in the high perfusion regime, in which it is purely permeability weighted. Outside of these two boundary regimes, although they may fit the data, the eTM and TM are not suitable for the pharmacokinetic analysis of DCE curves and may lead to misinterpretation of the results [132].

The case of negligible concentration of the contrast agent in the interstitium ($C_e \ll C_p$), which can occur due to a small PS or to large v_e, leads to the so called uptake models. These models assume a negligible back-flux of the contrast agent from the interstitium to the plasma space, which can be incorporated into the 2XCM and TH models by setting $\mathrm{PS} \cdot C_e(t) = 0$, into the AATH model by setting $\mathrm{PS} \cdot C_e(L,t) = 0$, and into the DP model by setting $\mathrm{PS} \cdot C_e(x,t) = 0$. In all cases, the parameters F_p, PS, and v_p can be derived, while the separate estimation of v_e is no longer possible. These models are mainly applicable in case of negligible extravasation of the contrast agent in the interstitium, such as in the case of intact BBB [154], [155] or trapping of the contrast particles [156], or when the acquisition window is not long enough to observe the contrast washout [128]. A particular case of uptake-model is the Patlak model [154], in which the further assumption of highly perfused tissue ($F_p \approx \infty$) is made. This produces the following solution:

$$C_t(t) = v_p C_p(t) + K^{\mathrm{trans}} * C_a(t). \tag{50}$$

Due to the assumptions of infinite flow, the intravascular concentration can be considered equal to the arterial concentration ($C_p(t) \equiv C_a(t)$), and K^{trans} is equivalent to PS. This model provides a separate estimation of v_p and K^{trans}, and it is particularly attractive because it can be linearized by defining two new variables $X(t)$ and $Y(t)$ as [12]

$$X(t) = \frac{\int_0^t C_a(\tau)d\tau}{C_a(t)}, \qquad Y(t) = \frac{C_t(t)}{C_a(t)} \tag{51}$$

leading to

$$Y(t) = v_p + K^{\mathrm{trans}} X(t). \tag{52}$$

Provided that the model assumption are met, the Patlak method is very suitable for data analysis, as plotting $X(t)$ versus $Y(t)$ produces a straight line with slope K^{trans} and intercept v_p.

One common drawback of all the models presented so far is the assumption of the AIF as input concentration in the capillaries; however, the AIF is usually sampled in a large artery more upstream, disregarding any effect of delay and dispersion due to the passage of the contrast bolus through the microvascular bed. While a simple delay can be corrected for by estimating the bolus arrival time (BAT), including dispersion effects is more complicated and requires explicit modeling of the contrast vascular transport [157]–[159]. Considering (29), the actual $C_a(t)$ can be seen as a convolution of the AIF with the vascular distribution of transit times function $r_a(t)$ as

$$C_a(t) = \text{AIF}(t) * r_a(t). \tag{53}$$

As a result, the measured tissue concentration can be expressed as

$$C_t(t) = \frac{F_p}{V_T}\text{AIF}(t) * r_a(t) * R(t). \tag{54}$$

For instance, by modeling the vascular bed as a well-mixed compartment, with an impulse response represented by a single exponential decay, Calamante *et al.* [157] derived the following expression for $r_a(t)$:

$$r_a(t) = e^{-t/\text{MTT}} \tag{55}$$

where MTT is the vascular mean transit time.

Other possible solutions for $r_a(t)$ are the Gaussian transport model [158] described as

$$r_a(t) = \frac{2\beta}{\sqrt{\pi}}e^{-\beta^2 t^2} \tag{56}$$

and the Gaussian residue model [158] described as

$$r_a(t) = 2\beta^2 t e^{-\beta^2 t^2}. \tag{57}$$

Based on (5), the effective MTT can be calculated as $\text{MTT} = 1/2\beta$ in (56), and as $\text{MTT} = \sqrt{(\pi)/(2 * \beta)}$ in (57).

Although modeling of the vascular transport requires the estimation of extra parameters, it may provide a more accurate description of the system and an additional characterization of the vascular tree. However, Calamante *et al.* [157] concluded that the simpler model represented by a single exponential decay [(54)] was sufficient for characterization of vascular dispersion in the cases studied.

Beside the delay and broadening effects, which may or may not be accounted for, the measurement of the AIF carries additional issues that may lead to errors in the estimated parameters. For instance, the partial-volume effect, arising when the AIF is measured in an ROI which also includes the vessel wall or surrounding tissue, may cause an underestimation of the vascular input [128], [160]. Moreover, in DCE-MRI, other sources of error in the measurement of the AIF are represented by inflow effects and by the nonlinear relationship between signal enhancement and contrast concentration. The former refers to the fact that protons flowing into the imaging volume have not experienced the same excitation as the stationary tissue, and thus have not yet reached the equilibrium magnetization. This results in an apparent decrease in the longitudinal relaxation time, leading to an increase in the signal, and thus to an overestimation of the AIF [161], [162]. The latter arises when linearity is assumed in the conversion from signal intensity to contrast concentration. Since the concentration in the arteries can be very high, the concentration regime of the linear conversion can be exceeded, thus leading to a underestimation of the AIF [128]. This problem can be overcome by the use of a dual-bolus injection technique, whereby the contrast agent is administered in two half doses with the aim of avoiding the risk of signal nonlinearities and saturation in the arterial signal [163].

To avoid these issues, a reference region (RR) model was proposed by Yankeloov *et al.* [130], which provides an equation for the estimation of K^{trans} and v_e by comparing the CTCs in the tissue of interest with those of a reference tissue, eliminating the need for the direct measurement of the AIF.

Alternatively, Mischi *et al.* [164] proposed a local characterization of $C_p(t)$ by modeling the bolus dispersion in the microvascular bed as a convective-dispersion process. Based on the adiabatic approximation [125], they combined the mLDRW solution to the convective-dispersion equation in (20) with the TM [(49)], thus obtaining the so called reduced dispersion model (RDM) as

$$C_t(t-t_0) = A\left(\sqrt{\frac{\kappa}{2\pi(t-t_0)}}e^{-\frac{\kappa}{2(t-t_0)}(t-t_0-\mu)^2}\right) * \left(e^{-k_{ep}t}\right) \tag{58}$$

where $A = \text{AUC} \cdot K^{\text{trans}}$.

The case of non-negligible capillary contribution to the total tissue concentration is also taken into account by combining (21) with the eTM [(49)], leading to the full dispersion model (FDM) given below

$$C_t(t-t_0) = B\left(\sqrt{\frac{\kappa}{2\pi(t-t_0)}}e^{-\frac{\kappa}{2(t-t_0)}(t-t_0-\mu)^2}\right) + A\left(\sqrt{\frac{\kappa}{2\pi(t-t_0)}}e^{-\frac{\kappa}{2(t-t_0)}(t-t_0-\mu)^2}\right) * \left(e^{-k_{ep}t}\right) \tag{59}$$

where $B = \text{AUC} \cdot v_p$.

Although the separate estimation of K^{trans} and v_p is no longer possible, these models include the effects of bolus delay and dispersion, and provide a local characterization of both the microvascular architecture by the dispersion parameter κ, and the microvascular permeability by the leakage parameter k_{ep}, without the need for a direct measurement of the AIF.

To summarize, several models for the assessment of perfusion, permeability, vascularity, and cellularity with DCE-CT and DCE-MRI have been presented. They differ in the level of complexity, the underlying assumptions, the regimes in which they are valid, and the parameters they are able to estimate (see Table III). The choice of a suitable pharmacokinetic model able to describe the measured CTC is dependent on several factors including acquisition settings and tissue hemodynamic features. Therefore, attention must be taken in the choice of the most appropriate model in order to avoid misinterpretation of the results.

TABLE III
SUMMARY OF QUANTITATIVE MODELS AVAILABLE FOR THE ANALYSIS OF DCE-MRI AND DCE-CT DATA

Model	Estimated parameters	Extra measurement/estimation	Ref.
DP	F_p, v_p, PS, v_e	AIF[1], BAT[2]	[131]
TH	F_p, v_p, PS, v_e	n.a.[3]	[134]
AATH	F_p, v_p, PS, v_e	AIF, BAT	[125]
2XCM	F_p, v_p, PS, v_e	AIF, BAT	[137]
eTM	K^{trans}, v_p, v_e	v_e	[145]
TM	K^{trans}, v_e	AIF, BAT	[127]
Patlak	K^{trans}, v_p	AIF, BAT	[154]
RR	K^{trans}, v_e	BAT, $C^4_{RR(t)}$	[130]
RDM	A, k_{ep}, κ, μ, t_0	none	[164]
FDM	A, B, k_{ep}, κ, μ, t_0	none	[164]

[1] AIF, Arterial input function; [2] BAT, Bolus arrival time; [3] n.a., not available; [4] $C_{RR}(t)$, Concentration time course measured in a RR.

III. CLINICAL APPLICATIONS

Quantitative assessment of the hemodynamic changes in the microvasculature associated with tumor angiogenesis is attractive for several clinical applications, which are discussed hereafter.

A. Lesion Detection and Characterization

Detection of cancer with conventional imaging can be challenging in certain organs and for certain tumor types, because tumor tissue does not always show peculiar features that enable its distinction from healthy tissue [165]. Moreover, when a suspicious mass is detected, its classification as benign or malignant is even more challenging. For instance, prostate cancer on conventional US images is generally associated with a hypoechoic appearance, but it can also appear iso- or hypoechoic [44], [72], [166]. In anatomic T2*-weighted MR images, the signal intensity of prostate cancer often overlaps with benign lesions such as hyperplasia, prostatitis, scars, and atrophy, making cancer detection difficult, especially in the central gland [167], [168]. In the liver, metastasis may remain hidden on standard anatomic CT images before they reach a detectable size [12]; with conventional US, lesions with isoechoic appearance or smaller size can often be overlooked [169], [170], and fat infiltration and fatty sparing may resemble lesions [171]. In the breast, multifocal lesions and tumors with confusing anatomy may remain undetected with structural MR imaging [44], while with conventional US the detection is limited by the size of the lesion. Another challenging assessment is represented by tumor grade, which has shown to correlate with tumor aggressiveness and prognosis [20], [21]. Estimation of cellular differentiation is thus important for predicting treatment response and for determining the most suited therapeutic strategy.

Due to the presence of tumor angiogenesis, the vasculature of malignant lesions differs from that of normal tissue and benign lesions, and is characterized by tortoise, irregular, and leaky vessels mainly concentrated in the tumor periphery [11]. As a result, enhanced imaging that is able to assess vascular functionality and morphology can yield improved cancer detection and localization. Moreover, quantitative imaging biomarkers of tumor angiogenesis have been shown to correlate with MVD count and tumor grade [21], thus angiogenesis imaging may also play an important role for lesion characterization and tumor grading.

Several studies have shown that DCE-US can improve the diagnosis of liver [171], [172], ovarian [173], [174], breast [175]–[177], kidney [178], [179], pancreas [180], and prostate cancer [181], by highlighting differences in the hemodynamic patterns and in quantitative perfusion parameters between healthy and cancerous tissue. In a study by Xu *et al.* [182], semiquantitative DCE-US parameters, such as WIT and MTT evaluated from a log-normal model fit, were able to differentiate between low risk, and intermediate and high risk prostate cancer in the inner gland. The use of contrast agents has also shown to improve hepatic lesions diagnosis compared to unenhanced imaging with MRI [183] and CT [184], and the literature suggests DCE-MRI to provide added diagnostic value and to improve tumor staging with respect to conventional structural T2*-weighted imaging in prostate [185] and breast cancer [14]. In addition, DCE-MRI has found an important role in the detection and characterization of lung [186], pancreatic [187], [188], cervical [189], head and neck [190], kidney [191], and brain tumors [192]. However, the interpretation of quantitative perfusion parameters may be contradictory and may depend on the specific organ. For instance, in the kidney [191] and pancreas [187], [188], quantitative perfusion parameters such as plasma flow, extraction fraction, and K^{trans} were significantly lower in tumors than in normal tissue; while in the prostate [193], [194] and breast [195], [196], tumor tissue typically shows higher perfusion parameters than normal tissue. Perfusion CT has shown to be a promising tool for diagnosis and characterization of several types of tumors, including liver, brain, rectal, lung, gastric, kidney, head and neck, and neuroendocrine cancer [197]–[199]. Quantitative perfusion CT parameters such as blood flow, blood volume, and K^{trans}, estimated with the Patlak approach, have been shown to correlate well with the MVD count in renal cell carcinoma [199]; a study by Ippolito *et al.* [200] demonstrated that quantitative perfusion CT parameters, such as hepatic perfusion, portal perfusion, blood volume, and TTP, evaluated with a dedicated quantitative software, differed significantly between hepatocellular carcinoma and surrounding liver tissue.

These studies show the great potential of quantitative angiogenesis imaging for tumor detection, characterization and grading, which are fundamental for cancer diagnosis and therapeutic decision making.

B. Focal Treatment: Patient Selection, Intervention Guidance and Treatment Follow Up

Currently, minimally-invasive focal therapies are available to treat localized tumors in several organs, such as prostate, breast, pancreas, kidney, uterus, bone, cervix, brain, head and neck, and liver [201]–[203]. Available treatments include focalized radiation therapy (dose-painting) [147], cryotherapy [204], irreversible electroporation [205], photodynamic therapy [206], brachytherapy [204], and a number of thermal ablative techniques [201], [206], [207]. These therapies represent a valuable alternative to radical treatment, which is inherently more invasive and carries a higher morbidity. However, their efficient use requires reliable cancer localization and accurate tumor

border delineation. As discussed in [208], one of the major limitation in the use of focal therapy for localized prostate cancer, especially for treatment planning and patient selection, is due to the lack of reliable imaging for accurate tumor localization and caractherization. Improvements can be obtained with use of contrast-enhanced imaging: using DCE-MRI and DCE-US led to an increase in specificity and sensitivity in tumor detection compared to unehanced imaging [208]. In a study by Kneeshaw *et al.* [209], it was shown that semiquantitative DCE-MRI in breast cancer has higher sensitivity and provides better cancer localization than other modalities, suggesting its use for accurate tumor delineation and staging prior to surgery. Similarly, in a consensus panel on the role of MRI in focal therapy for prostate cancer, it was concluded that conventional structural MRI without functional imaging is not sufficient for accurate diagnosis and cannot provide reliable measurement of tumor volume in small tumors eligible for focal therapies [210]. In thermal ablation therapy, contrast CT is recommended immediately after treatment for its ability to discriminate between ablated and residual viable tumor [211]. These studies suggest that functional contrast-enhanced imaging may improve treatment planning in the preoperative phase, treatment guidance during intervention, and treatment monitoring in the follow-up phase, by providing more accurate tumor localization and staging, and better discrimination between treated and untreated tissue.

C. Prediction, Assessment and Monitoring of Response to Therapy

Quantitative angiogenesis imaging also holds great potential in predicting and monitoring response to chemo-, vascular-disrupting, and antiangiogenic therapies. Traditional criteria for evaluation of therapeutic response mainly rely on tumor size evaluated by conventional imaging methods. Through a bi-dimensional measurement of the lesion, the World Health Organization criteria categorizes the response to treatment as complete response, partial response, disease progression, or stable disease. In an attempt to simplify the evaluation, the response criteria in solid tumors (RECIST) were later introduced, dividing the response into the same categories by using a one-dimensional measurement. RECIST integrates now the most used criteria in clinical trials [20]. Other commonly used indices of therapeutic efficacy relate to patient survival time. Examples are disease-free, progression-free (PFS), and overall survival (OS) time. However, patient survival time and dimension-based assessment criteria present some limitations especially in evaluating the response in the early phases of treatment [71], [212], [213]. In chemotherapy, cytotoxic drugs are used to target rapidly dividing cells, which are typical of cancerous tissue, leading to complete tumor depletion or reduction in size. Nevertheless, alteration in tumor size is a relatively late event which is long anticipated by functional changes. The limitations of tumor size assessment are even more pronounced in the evaluation of novel antiangiogenic therapies, which act by preventing the growth of new blood vessels and/or by disrupting existing tumor vasculature, thus reducing the number, area, and volume of tumor vessels and inhibiting tumor growth [20], [71]. In this case, the effect of treatment is cytostatic rather than cytotoxic and does not necessarily lead to alterations in tumor size [20], [179], [212]. As a result, additional assessment of functional changes is crucial to monitor the therapeutic response, and may help to identify nonresponders in the early stages of treatment, providing the clinician with the possibility to adjust the therapeutic strategy accordingly. Furthermore, since tumor perfusion is a surrogate marker of tissue viability [67], [213], [214], assessing the vascular function could also represent a powerful pretreatment tool to predict therapeutic outcome, and thus may guide patient selection in order to avoid unnecessary treatment.

In this context, quantitative angiogenesis imaging represents a valid option to simultaneously evaluate structural changes, such as tumor size and vascular architecture, and functional changes, such as perfusion and permeability. A number of preclinical and clinical studies have demonstrated the feasibility of DCE-US for prediction of tumor response [20], [213], [215]. DCE-US derived qualitative, semiquantitative, and quantitative perfusion parameters were able to provide an early prediction of therapeutic outcome in accordance with later assessment using traditional criteria, in renal cell carcinoma [216], [217], hepatocellular carcinoma [212], and gastrointestinal tumor [218]. However, results are contradictory and some studies showed that, although DCE-US is able to provide reproducible and sensitive parameters for the assessment of vascular changes in response to antiangiogenic therapy (e.g., fractional blood volume measured with the destruction replenishment technique, and peak intensity and AUC estimated after LDRW model fitting), these did not correlate with long-term assessment criteria, such as RECIST and PFS [219]. Similarly, in a review of clinical trials of antiangiogenic and vascular disrupting agents employing DCE-MRI for evaluation of drug efficacy it was shown that although K^{trans} showed a dose-dependent reduction, it did not correlate with clinical response [220]. On the other hand, a comprehensive evaluation of studies involving DCE-CT and DCE-MR imaging biomarkers of outcome following VEGF inhibition therapy in renal cancer and high grade gliomas showed strong evidence that changes in quantitative pharmacokinetic parameters such as K^{trans} correlate with PFS and OS [221]. In a study evaluating the potential of DCE-CT as early biomarker of response to antiangiogenic treatment in metastatic renal cell carcinoma [222], quantitative parameters such as blood flow and volume immediately after treatment showed a significantly higher drop in those patients later classified as responders than in nonresponders. The ability of quantitative DCE-CT parameters to detect early tumor response was also demonstrated by Tacelli *et al.* [223], who evaluated tumor vascular volume and extravascular flow (K^{trans} multiplied by the total tissue volume, evaluated from Patlak analysis) in patients with non-small cell lung cancer undergoing antiangiogenic chemotherapy before, and after one, three, and six cycles of therapy: DCE-CT quantitative parameters were able to assess early changes in tumor vascularity which correlated with responders and nonresponders assessed by RECIST criteria.

Angiogenesis imaging, which is able to simultaneously evaluate structural and functional changes in tumor vascularity, holds great promises for the evaluation of response to chemotherapy, antiangiogenic, and vascular-disrupting therapies, especially for prediction of therapy outcome, which may aid patient selection,

and evaluation and monitoring of early response, possibly leading to a better management of the therapeutic strategy. However, further research is needed to establish the suitability, reproducibility, and reliability of quantitative angiogenesis imaging biomarkers for these purposes.

D. Drug Development

The development of antiangiogenic and vascular-targeting therapies is a relatively new and very active field of oncologic research. Many new drugs are developed and tested every year, and their efficacy, biological effects, and mechanism of action are not yet completely understood. In this context, quantitative angiogenesis imaging may represent an important tool to evaluate new drugs already in preclinical and clinical trials. During the drug development process, a drug is first tested in nonhuman subjects (preclinical phase), then the drug pharmacodynamics (phase 0), tolerability, and safety (phase I, II, III), as well as drug efficacy and effectiveness (phase II, III), are tested on humans [224]. Imaging plays an important role especially in phase 0, to clarify the mechanism of action of the new drug, and in phases I and II, for early evaluation of drug safety and efficacy [224], [225]. In this context, quantitative measurement of the changes in blood flow, volume, and vessel permeability may represents a valid option to evaluate the drug effect on tumor microvascular functionality and structure [224], [225].

A phase II clinical trial evaluating the efficacy and safety of the antiangiogenic agent sunitinib (VEGF-R2 and PDGFR-beta tyrosine kinase inhibitor) in patients with advanced hepatocellular carcinoma showed that quantitative DCE-MRI biomarkers such as K^{trans} and k_{ep}, estimated by application of the TM, might be indicative of response and resistance to the agent, and thus they may be suitable for early evaluation of drug efficacy [226]. In a phase I study investigating the efficacy of treatment of solid tumors with a combination of antiangiogenic and chemotherapeutic drugs (sorafenib, targeting Raf kynases and VEGF receptors; and dacarbazine, alkylating agent) [227], DCE-US semiquantitative parameters related to the blood volume (peak intensity, AUC, area under the wash-in, area under the wash-out) and the rate of blood flow (WIR) were used to evaluate drug efficacy at three months after treatment, showing to be significantly predictive of therapy outcome evaluated with the RECIST criteria. The hemodynamic response in chest and abdomen tumors treated with a combination of antiangiogenic drug (cediranib, targeting VEGFR2; and gefitinib, inhibiting EGFR) was evaluated with perfusion CT in a phase I clinical trial [228]: quantitative CT parameters showed significant decrease in liver tumor tissue, while there was no change in normal liver parenchyma. However, no correlation was found between changes in tumor perfusion and tumor size, arguing that volume changes may not be a suitable criterion to evaluate antiangiogenic drug efficacy.

In anticancer therapy research, there is an increasing interest in finding suitable imaging biomarkers for early evaluation of therapeutic response able to prove drug efficacy already during phase I, with the aim of accelerating the drug development process [224]. Currently, this is attained by objective criteria based on tumor size measurement such as RECIST. However, especially when the mechanism of action of a drug is cytostatic rather than cytotoxic, traditional criteria based on tumor size measurement are not suitable to evaluate drug efficacy, evidencing a need for new standardized criteria for assessment of therapeutic outcome. To this end, quantitative angiogenesis imaging biomarkers, able to assess both functional and structural changes in tumor vasculature, may represent a valid option. However, extensive research is needed to establish which parameters and imaging modalities are more suitable for each specific agent and tumor type.

IV. Discussion

The need for earlier and improved cancer diagnosis, localization, and characterization, as well as for reliable methods for early evaluation of therapeutic response have led to the development of several imaging modalities able to assess the structural and functional vascular changes associated with tumor angiogenesis. Selection of the best suited imaging modality and protocol, contrast mechanism, and data analysis varies from case to case, and depends on several aspects, including accessibility of instrumentation, patient characteristics, and the biological features of the organ or lesion to be investigated. A comparison of the presented models, summarizing the main assumptions, applicability, advantages, limitations, and complexity is given in Table IV for DCE-US and in Table V for DCE-MRI/CT.

In DCE-US, although the constant infusion protocol permits perfusion quantification in multiple planes, its implementation is more complicated, requiring the use of an injection pump, the attainment of a steady-state level infusion rate, and a more complex imaging sequence whereby the MI needs to be switched from low to high [41]. As a result, bolus injection protocols have been used and validated more extensively. The available models for the analysis of a bolus pass show comparable complexity and applicability. However, besides the advantage of having a physiological basis, which takes into account the underlying microvascular structure, the LDRW model has shown more accurate data fit both *in vivo* [68], [91] and *in vitro* [229], and thus it should be generally chosen as the preferred model for DCE-US bolus data fitting.

In DCE-MRI and DCE-CT, more complex models (DP, TH, AATH, 2CXM) provide a more accurate description of the underlying tissue structure, although disregarding dispersion and diffusion effects due to the bolus transport from the sampling artery to the microvascular bed, and permit the separate estimation of flow and permeability. However, higher model complexity also translates into higher demands in terms of temporal resolution and computational requirements. Since distributed models do not assume instant contrast mixing, a temporal resolution smaller than 1.5 s is suggested for accurate parameter estimation [142], [220]. In addition, the computational demands generally increase with increasing dimension of the parameter search space, making the choice of the fitting strategy more critical than the SNR requirements, which in turn do not show great influence on the accuracy of the parameter estimates [142], [230]. In general, an analytical closed-form model solution, which is continuous and differentiable in the time domain, is more

TABLE IV
COMPARISON OF QUANTITATIVE MODELS USED IN DCE-US

Model	Assumptions	Applicability (types of tissue)	Remarks	Complexity
Lognormal	- Bolus-injection	*Wide*. Any perfused tissue.	- Extensive validation	*Medium*. Estimation of $3 + 1^5$ parameters.
Gamma-variate	- Bolus-injection	*Wide*. Any perfused tissue.	- Extensive validation - Analytical solution not in closed form	*Medium*. Estimation of $3 + 1^5$ parameters.
LDRW	- Bolus-injection - IV space as plug-flow system (infinitely-long straight tube) - Fluid velocity and contrast diffusion coefficient spatially independent	*Wide*. Any perfused tissue.	- Extensive validation - Solution derived from physiological description of the dilution process	*Medium*. Estimation of $3 + 1^5$ parameters.
FTP	- Bolus-injection - IV space as plug-flow system (infinitely-long straight tube) - Fluid velocity and contrast diffusion coefficient spatially independent - Recirculation not allowed	*Wide*. Any perfused tissue.	- Limited validation - Solution derived from physiological description of the dilution process	*Medium*. Estimation of $3 + 1^5$ parameters.
Lagged Normal	- Bolus-injection - Concentration in large artery modeled by a Gaussian density function and microvascular bed as a series of well-mixed compartments	*Wide*. Any perfused tissue.	- Limited validation	*Variable*. Depending on the number of compartments.
Wei mono - exponential	- Constant infusion - IV space as single compartment	*Wide*. Any perfused tissue.	- Extensive validation - US field properties and vascular tree inhomogeneity not modeled	*Low*. Estimation of $2 + 1^5$ parameters.
Arditi/Hudson	- Constant infusion - Multiple vessels with different flows and entry angles - US field properties included	*Wide*. Any perfused tissue.	- Limited validation - US field properties and vascular tree inhomogeneity modeled - Extra measurement for US beam properties required	*High*. Estimation of $4 + 1^5$ parameters, and measurement of US field properties required.

[5] The time of appearance t_0 may be estimated separately to reduce the dimension of the parameter search space in the recursive curve-fitting routine.

favorable for curve fitting because it provides a continuous error function, leading to improved estimation precision [142], [230].

Although simpler models (eTM, TM, Patlak) are computationally less demanding and permit stretching the temporal resolution to 6 s or higher [142], [231], 1-s resolution AIF measurement is still suggested in order to capture the fast dynamics of the vascular phase and provide accurate estimates, especially for the vascular parameters [231], [232]. In fact, the measurement of the AIF is generally critical, prone to several sources of measurement errors (saturation, partial volume effects, inflow effects, nonlinear calibration) [132], [160]–[162], and relying on strong assumptions (AIF in tissue to be the same as in the sampling artery) [157], [158], [164], which eventually may translate into errors in the estimated parameters. If the AIF cannot be measured or estimated reliably, the use of models such as the RR, in which the AIF is estimated from a reference tissue, or the FDM and RDM, which also include the bolus transport from the injection to the detection site in the model description, are thus favorable.

In general, when simpler models (eTM, TM, Patlak) are employed, special attention is required to ensure that the investigated tissue complies also with the adopted simplifying assumptions on tissue characteristics [132]. Although these models have found widespread application in the past years, their use was mostly dictated by the limitations in the attainable resolution and computational requirements. Thanks to continuous technological advances, nowadays these requirements are met more easily; therefore, the application of more complex models, which enables relaxing the assumptions on the vascular transport and tissue structure, and generally improve fit accuracy [141], [164], [233], [234], is highly suggested. A cohort of studies has in fact shown that more complex models (AATH, 2XCM) have better performance for temporal sampling of 4 s or smaller [141], [144], [233], [234], while simpler models (eTM, TM, Patlak) perform better for larger temporal sampling [235], [236].

Besides the temporal resolution and the AIF, several other aspects of DCE-MRI/CT acquisition (e.g., baseline length, scan duration, SNR, signal drift, T1 mapping, field inhomogeneity, contrast injection rate, motion artifacts) may eventually influence estimation accuracy, but unfortunately they have been quantitatively addressed only in few isolated studies [235], [237]–[241], and in some cases with contradictory findings. Errors in the measured native tissue T1 during DCE-MRI calibration appear to have a critical impact on the estimated pharmacokinetic parameters [238], [240], while scan duration seems not to have a great influence [235], [237]. Although higher errors in the estimated parameters are reported for decreasing SNR, reliable estimates can still be obtained, provided that the SNR level is sufficient for the chosen model [142], [237], [241].

TABLE V
COMPARISON OF QUANTITATIVE MODELS USED IN DCE-MRI AND DCE-CT

Model	Assumptions	Applicability (types of tissue)	Remarks	Complexity
DP	- IV space as plug-flow system - EV space as distributed system - F_p and PS spatially independent	*Wide*. Any perfused tissue.	- Separate estimation of F_p and PS - Demanding temporal resolution requirements - Extra measurement of the AIF needed - Analytical solution in the time domain not in closed-form - Very limited validation	*High*. Estimation of 4+1[5] parameters and separate estimation of the AIF.
TH	- IV space as plug-flow system - EV space as well-mixed compartment	*Wide*. Any perfused tissue.	- Separate estimation of F_p and PS - Demanding temporal resolution requirements - No analytical solution available in the time domain. - Extra measurement of the AIF needed - Very limited validation	*High*. Estimation of 4+1[5] parameters and estimation of the AIF.
AATH	- IV space as plug-flow system - EV space as well-mixed compartment - Exchange occurring only at the venous end (adiabatic approximation)	*Wide*. Any perfused tissue.	- Separate estimation of F_p and PS - Demanding temporal resolution requirements - Extra measurement of the AIF needed - Analytical closed-form in the time domain is a piecewise function - Limited validation	*High*. Estimation of 4+1[5] parameters and separate estimation of the AIF.
2CXM	- IV and EV spaces as well-mixed compartments	*Wide*. Any perfused tissue.	- Separate estimation of F_p and PS - Extra measurement of the AIF needed - Analytical closed-form available - Limited validation	*Medium high*. Estimation of 4+1[5] parameters and separate estimation of the AIF. Differentiable closed-form solution available.
eTM	- $F_p \approx \infty$ or $v_p \approx 0$	*Medium*. Well perfused or weakly vascularized tissue (brain, head and neck, breast, lung, renal, prostate, rectal, cervical, oral, pancreatic)	- Extra measurement of the AIF needed - Extensive validation	*Medium low*. Estimation of 3+1[5] parameters and separate estimation of the AIF.
TM	- $F_p \approx \infty$ - $v_p \approx 0$	*Limited*. Well perfused and weakly vascularized tissue (brain, breast, prostate, cervical, oral, pancreatic)	- Extra measurement of the AIF needed - Extensive validation	*Low*. Estimation of 2+1[5] parameters and separate estimation of the AIF.
Patlak	- $C_e \ll C_p$	*Limited*. Tissue with large EV space or low PS (brain, renal)	- Extra measurement of the AIF needed - Model linearization possible	*Very low*. Estimation of 2+1[5] parameters, and separate estimation of the AIF.
RR	- $F_p \approx \infty$ - $v_p \approx 0$	As TM	- AIF estimated from a reference tissue - Limited validation	*Low*. Estimation of 2+1[5] parameters, and measurement of $C_{RR}(t)$.
RDM	- $F_p \approx \infty$ - $v_p \approx 0$	As TM	- No extra measurement required - Delay and dispersion of the AIF included in the model - Limited validation	*Medium*. Estimation of 5 parameters.
FDM	- $F_p \approx \infty$ or $v_p \approx 0$	As eTM	- No extra measurement required - Delay and dispersion of the AIF included in the model - Limited validation	*High*. Estimation of 6 parameters.

[5] The time of appearance t_0 may be estimated separately to reduce the dimension of the parameter search space in the recursive curve-fitting routine.

In fact, model selection is not only dependent on the specific tissue conditions, but also on the available data: the search is not for the best model *per se*, but rather for the most appropriate model given the data. When the number of parameters is too large or the SNR is too low, the data might not contain sufficient information for accurate estimation of all parameters, potentially leading to overfitting; this occurs when a mathematical model tends to describe random errors or noise instead of the relationship underlying the data [242]. Therefore, the best model should be selected in a balance between fit accuracy and parsimony, i.e., the concept of using the least number of parameters able to describe the data adequately [242], [243].

A probabilistic approach to the problem of model selection, whereby several models of different complexity are compared and graded, is thus recommended. When the models are nested (i.e., each model is obtained from a more complex by reducing the number of terms), log-likelihood tests can be performed to evaluate the probability of one model to describe the data better than the other [242], [243]. For non-nested models, metrics such as the Akaike information criterion (AIC), the Bayesian information criterion (BIC), or the minimum description length (MDL) can be used, which grade the models based on fitting accuracy but also introduce a penalty for the number of parameters [242], [243].

Quantification and standardization are fundamental to compare performance between imaging modalities, protocols, and parameters. Unfortunately, in most clinical studies only qualitative or semiquantitative analysis has been performed. Although qualitative and semiquantitative parameters can be calculated relatively easily [244], they are dependent on several factors, including contrast concentration, patient characteristic, machine settings, and operator experience [14]. As a result, non or semiquantitative analysis may lack accuracy and hamper standardization, limiting the exchange of information between different institutions. On the other hand, accurate and reliable calculation of quantitative parameters can be challenging because it requires the use of mathematical models of variable complexity, careful signal calibration, and strict protocols. However, quantification presents advantages that may overcome the limitations of qualitative and semiquantitative analysis. Quantitative assessment is less operator- and machine-dependent, and it can be fully automated, thus allowing for the implementation of multicenter trials and for standardization of protocols. The latter facilitates a reliable comparison of findings between different studies and centers.

Comparing single imaging modalities, DCE-US presents several advantages for assessing tumor angiogenesis. The intravascular character of the adopted contrast allows disregarding diffusion and leakage across the vascular endothelium, thus making DCE-US well suited for perfusion quantification. With the introduction of the latest generation of microbubbles and of new contrast-specific imaging techniques, DCE-US enables real-time detection of blood flow in vessels as small as 40 micron [69], [71]. In addition to high spatial and temporal resolution, other advantages of DCE-US are represented by portability, availability, cost-effectiveness, and the absence of ionizing radiation [245], which make this modality very attractive for screening, focal-treatment follow up, and therapy monitoring, where frequently repeated measurements are needed. Moreover, US imaging has an established user base and is already routinely used in clinical practice for screening and diagnosis of cancer in several organs (e.g., liver, breast, ovaries) [171], [246]–[249].

Regarding the limitations, US has poor accessibility to certain anatomical regions, such as the pulmonary and cerebral areas, and shows reduced performance in deeper organs [20]. In addition, US imaging is highly dependent on the operator ability and experience. Furthermore, quantification with DCE-US is more challenging, being affected by acoustic attenuation, patient and operator variability, US scanner settings, and microbubbles characteristics [250], [251]. The lack of reproducibility in quantitative analysis makes standardization challenging; as a result, validation of quantitative DCE-US parameters against available biomarkers of tumor angiogenesis has been limited to a few studies so far [252], [253]. Moreover, unlike DCE-MRI and DCE-CT, in which multiple planes can be investigated simultaneously with a single bolus injection, a major limitation of DCE-US, currently being mostly a 2-D technique, resides in that only one plane can be investigated for each injected bolus, thus increasing the risk of missing out-of-plane malignancies. Finally, since UCAs are purely intravascular tracers, capillary permeability and leakage cannot be investigated.

The iodinated and gadolinium-based contrast agents adopted in DCE-CT and DCE-MRI, respectively, are able to cross the vascular endothelium and extravasate into the interstitium, thus providing an opportunity to assess changes in microvascular permeability and leakage space, which can be related to cancer angiogenesis. However, extravasation increases the complexity of contrast transport modeling and makes parameter estimation more challenging.

The main advantages of DCE-CT include rapid scanning, high resolution, whole body 3-D coverage, widespread availability at reasonable costs [245], [254], [255], and the linear relationship between contrast agent concentration and signal intensity [14], [255], which facilitates quantification. The acquisition of good quality DCE-CT data is a relatively robust process and reproducibility of quantitative parameters in several cancer types has been documented [197]. However, DCE-CT has poor soft-tissue contrast [255], and it is affected by a number of noise sources including photon noise, especially in hypovascular tumors, and partial volume effects [12], the extent of which is greater as the investigated ROI becomes smaller, such as for instance in the measurement of the AIF. Moreover, the major drawback of DCE-CT is represented by the use of ionizing radiation [14], [197], which increases cancer risk and, thus counterbalances the potential benefit of angiogenesis assessment, especially for treatment outcome monitoring whereby several repeated measurement are needed [14], [61], [256]. Finally, the use of iodinated contrast agent in patients with impaired renal function raises concerns because of the risk of contrast-induced nephrotoxicity [257].

DCE-MRI offers excellent soft-tissue contrast, high-spatial resolution, large depth of penetration, and good SNR [113], [245]. Although limited by high costs and restricted availability, DCE-MRI is becoming a standard examination for cancer diagnosis in several organs (e.g., prostate, breast) [44], [185], and the absence of ionizing radiation makes in principle this modality well-suited for screening, treatment follow up, and therapy monitoring [113], [258]. One major drawback of DCE-MRI is represented by the nonlinear relationship between contrast agent concentration and signal intensity [14], [24]. Gadolinium concentration can be quantified by acquiring maps of tissue T1 relaxivity prior to contrast injection and, then, applying nonlinear calibration [259]. However, the acquisition of T1 maps can be challenging and time consuming, and it requires careful calibration and correction for field inhomogeneity [120], [259]. As a result, T1 map calibration for absolute contrast quantification is rarely performed in clinical practice, limiting repeatability, reproducibility, and standardization of DCE-MRI [24]. In

addition, the use of different acquisition protocols and analysis methods, and the absence of consensus on the nomenclature of some pharmacokinetic parameters complicates the comparison of findings between studies and centers [14], [260]. Moreover, the use DCE-MRI is limited for organs with physiologic motion, such as the lungs and the liver [14], [24], [261], in patients with pacemakers and metallic implants [262], [263], and in patients with impaired kidney function due to agent toxicity [14]. Finally, DCE-MRI images can be affected by several noise sources including partial volume and inflow effects. The latter can be particularly critical in the acquisition of the AIF, where a small volume including an artery with high flow is imaged [130], [264].

V. Recommendations and Outlook

The introduction of novel targeted contrast agents may boost further advances in angiogenesis imaging with DCE-US and DCE-MRI. These new emerging agents are obtained by binding marker molecules (peptides, proteins, and antibodies) to the imaging agent to specifically target molecular expression of angiogenesis [265]–[268]. Typical molecular targets include VEGF receptors, key regulators of angiogenesis and vasculogenesis, and $\alpha_V\beta_3$ integrin, cell adhesion molecule mediating the migration of endothelial cells through the basement membrane during blood-vessel formation [269]. Contrast agents decorated with angiogenesis-targeting ligands remain attached to the areas in which the target molecule is upregulated, thus causing selective enhancement in DCE images, especially in the late phase after injection [266]. Mathematical modeling of targeted agents binding kinetics may give deeper insight on the physiological mechanisms underlying angiogenic processes and may provide more quantitative assessment of tumor angiogenesis. Currently, the feasibility of molecular imaging with DCE-US and DCE-MRI has been demonstrated [266], [268], and human studies are ongoing to demonstrate clinical utility and permit the translation of these novel agents for clinical applications [270], [271].

The long awaited introduction of four-dimensional (4-D) scanning in US imaging may overcome a major limitation of DCE-US. 4-D DCE-US allows observing the contrast kinetics in a volume rather than a single plane, enabling simultaneous perfusion quantification in multiple planes with a single bolus injection, similar to DCE-CT and DCE-MRI [72], [272].

Quantitative angiogenesis imaging requires proper model selection in order to ensure reliable parameter estimation, and thus, provide clinically useful information on the investigated organ. Due to the greater simplicity of the bolus-injection protocol, the proven fit accuracy, and its physiological basis, the LDRW model is recommended for assessment of angiogenic tumor vasculature with DCE-US.

In DCE-MRI/CT, the increased model complexity, due to the extravascular character of the adopted contrast agents, makes parameter estimation more sensitive to the acquisition protocol. When a reliable estimate of the AIF is available, models which allow for the separate estimation of flow and permeability, such as the 2XCM and AATH, are recommended, provided that the temporal resolution and SNR are sufficiently high. When these requirements are not met, a simpler model (eTM, TM, Patlak) should be chosen, based on the *a priori* knowledge on tissue properties and condition. When the AIF cannot be measured or estimated reliably, the FDM, or the simpler RDM or RR should be chosen, depending on the number of parameters that can be reliably estimated with the given temporal resolution and SNR; once again, attention should be paid to ensure that the investigated tissue condition complies with the underlying model assumptions. In general, the best practice would be to try several suitable models of different complexity and grade them through a proper probabilistic test (log-likelihood, AIC, BIC, MDL). This not only would provide the investigators with more certainty about the chosen model, but would also help expanding the scientific evidence on model selection for different organs and experimental conditions. Ideally, based on a systematic probabilistic evaluation, a decision table for model selection and guidelines for proper acquisition protocols could be implemented in consensus.

All the clinical imaging modalities have specific advantages and drawbacks, and no single technique can outperform the others in each and every case. For each specific case, choosing and applying consistently one imaging modality with a fixed protocol would be recommendable to allow intra and interpatient comparison and follow up. However, the synergetic use of multiple modalities can provide more reliable and accurate information than a single modality alone [273], [274]. In [273], morphological and functional features of angiogenesis were assessed in a rat bearing breast cancer bone metastasis by multimodality imaging: MRI and DCE-MRI were performed for high soft tissue contrast and quantification of blood volume, perfusion, and vessel permeability; CT angiography and DCE-CT for macrovessel architecture characterization and assessment of the microcirculation; and B-mode US, Doppler US, and DCE-US for evaluation of morphology and perfusion in soft tissue. Multimodal imaging is needed to overcome current limitations and to make efficient and integrated use of all the available information. It represents the future of angiogenesis imaging and of clinical diagnostic imaging in general [275], [276].

In conclusion, quantitative imaging of tumor angiogenesis has the potential to improve cancer diagnosis, focal treatment guidance and follow up, therapeutic-response prediction and monitoring, treatment decision making, and drug development. In the effort toward standardization of quantitative imaging, the Radiologic Society of North America organized in 2007 the Quantitative Imaging Biomarker Alliance (QIBA), whose mission was to improve the value and practicality of quantitative imaging biomarkers by reducing variability across devices, patients, and time [260], [277]. In response, QIBA is producing basic standards and protocols for several quantitative imaging techniques, including DCE-MRI [278], volumetric CT [279], and FDG-PET/CT [280]. Multimodal approaches will lead to more accurate and effective cancer characterization and management. Cooperation between clinicians and researchers of different institutions and organizations is crucial to improve the standardization of quantitative analysis, which is necessary to translate the great potential of angiogenesis imaging into the clinical routine.

References

[1] P. Camerliet, "Angiogenesis in life, disease and medicine," *Nature*, vol. 438, no. 15, pp. 932–936, 2005.

[2] I. S. Gribbestad *et al.*, "An introduction to dynamic contrast-enhanced MRI in oncology," in *Dynamic Contrast-Enhanced Magnetic Resonance Imaging in Oncology*. New York, NY, USA: Springer, 2005, pp. 1–22.

[3] G. Russo, M. Mischi, W. Scheepens, J. J. de la Rosette, and H. Wijkstra, "Angiogenesis in prostate cancer: Onset, progression and imaging," *BJU Int.*, vol. 110, no. 11c, pp. E794–E808, 2012.

[4] R. S. Kerbel, "Tumor angiogenesis: Past, present and the near future," *Carcinogenesis*, vol. 21, no. 3, pp. 505–515, 2000.

[5] Y. Li and P. J. Cozzi, "Angiogenesis as a strategic target for prostate cancer therapy," *Med. Res. Rev.*, vol. 31, no. 1, pp. 22–36, 2010.

[6] H.-C. Wu, C.-T. Huang, and D.-K. Chang, "Anti-angiogenic therapeutic drugs for treatment of human cancer," *J. Cancer Molecules*, vol. 4, no. 2, pp. 37–45, 2008.

[7] T. Jeswani and A. Padhani, "Imaging tumour angiogenesis," *Cancer Imag.*, vol. 5, no. 1, pp. 131–138, 2005.

[8] K. A. Miles, "Tumour angiogenesis and its relation to contrast enhancement on computed tomography: A review," *Eur. J. Radiol.*, vol. 30, pp. 198–205, 1999.

[9] S. A. Stacker, M. E. Baldwin, and M. G. Achen, "The role of tumor lymphangiogenesis in metastatic spread," *FASEB J.*, vol. 16, pp. 922–934, 2002.

[10] M. Dadiani, E. Furman-Haran, and H. Degani, "The application of NMR in tumor angiogenesis research," *Progress Nuclear Magn. Resonance Spectroscopy*, vol. 49, pp. 27–44, 2006.

[11] J. C. Miller, H. H. Pien, D. Sahani, G. A. Sorensen, and J. H. Thrall, "Imaging angiogenesis: Applications and potential for drug development," *J. Nat. Cancer Inst.*, vol. 97, no. 3, pp. 172–187, 2005.

[12] K. A. Miles *et al.*, "Application of CT in the investigation of angiogenesis in oncology," *Acad. Radiol.*, vol. 7, no. 10, pp. 840–850, 2000.

[13] M. Mischi, M. P. J. Kuenen, and H. Wijkstra, "Angiogenesis imaging by spatiotemporal analysis of ultrasound contrast agent dispersion kinetics," *IEEE Trans. Ultrason. Ferrelectr. Freq. Control*, vol. 59, no. 4, pp. 621–629, Apr. 2012.

[14] B. Turkbey, H. Kobayashi, M. Ogawa, M. Bernardo, and P. Choyke, "Imaging of tumor angiogenesis: Functional or targeted?" *Amer. J. Roengtenol*, vol. 193, pp. 304–313, 2009.

[15] N. Charnley, S. Donaldson, and P. Price, *Imaging Angiogenesis*, vol. 467, 2nd ed. New York, NY USA: Humana Press, 2009, sec. 25– 51.

[16] C. Cuenod, L. Fournier, D. Balvay, and J.-M. Guinebretie, "Tumor angiogenesis: Pathophysiology and implications for contrast-enhanced MRI and CT assessment," *Abdominal Imag.*, vol. 31, pp. 188–193, 2006.

[17] T. Barrett, M. Brechbiel, M. Bernardo, and P. L. Choyke, "MRI of tumor angiogenesis," *J. Magn. Resonance Imag.*, vol. 26, no. 235–249, 2007.

[18] J. Folkman, "Clinical applications of research on angiogenesis," *New Engl. J. Med.*, vol. 333, no. 26, pp. 1757–1763, 1995.

[19] T. Barrett, K. Hisataka, M. Brechbiel, and P. L. Choyke, "Macromolecular MRI contrast agents for imaging tumor angiogenesis," *Eur. J. Radiol.*, vol. 60, pp. 353–366, 2006.

[20] C. Marcus *et al.*, "Imaging techniques to evaluate the response to treatment in oncology: Current standards and perspectives," *Critical Rev. Oncol. Hematol.*, vol. 72, pp. 217–238, 2009.

[21] N. Weidner, J. P. Semple, W. R. Welch, and J. Folkman, "Tumor angiogenesis and metastasis - correlation in invasive breast carcinoma," *New Engl. J. Med.*, vol. 324, no. 1, pp. 1–8, 1991.

[22] R. D. Folkerth, "Descriptive analysis and quantification of angiogenesis," *J. Neuro-Oncol.*, vol. 50, pp. 165–172, 2000.

[23] E. Hannen and D. Riediger, "The quantification of angiogenesis in relation to metastasis in oral cancer: A review," *Int. J. Oral Maxillofacial Surg.*, vol. 33, pp. 2–7, 2004.

[24] T. Barrett and P. Choyke, *Imaging of Angiogenesis*. New York, NY, USA: Springer, 2008, sec. 28, pp. 321–332.

[25] M. E. Loveless and T. E. Yankeelov, *Dynamic Contrast Enhanced MRI: Data Acquisition and Analysis*. New York, NY, USA: Taylor & Francis, 2012, sec. 12, pp. 143–161.

[26] S. S. Abdelmoneim *et al.*, "Safety of contrast agent use during stress echocardiography," *JACC: Cardiovascular Imag.*, vol. 2, no. 9, pp. 1048–1056, 2009.

[27] C. Burtea, S. Laurent, L. Vander Elst, and R. N. Muller, "Contrast agents: Magnetic resonance," in *Handbook Experimental Pharmacology: Molecular Imaging* I, vol. 185. Berlin: Springer-Verlag, Pt 1, pp. 135–165, 2008.

[28] K. M. Hasebroock and N. J. Serkova, "Toxicity of MRI and CT contrast agents," *Expert Opinion Drug Metabolism Toxicol.*, vol. 5, no. 4, pp. 403–416, 2009.

[29] S. B. Feinstein *et al.*, "Contrast enhanced ultrasound imaging," *J. Nucl. Cardiol.*, vol. 17, no. 1, pp. 106–115, 2010.

[30] I. Fox, "History and developmental aspects of the indicator-dilution technic," *Circular Res.*, vol. 10, pp. 381–392, 1962.

[31] S. Jhanji, J. Dawson, and R. M. Pearse, "Cardiac output monitoring: Basic science and clinical application," *Anasthesia*, vol. 63, no. 2, pp. 172–181, 2008.

[32] K. Zierler, "Indicator dilution methods for measuring blood flow, volume, and other properties of biological systems: A brief history and memoir," *Ann. Biomed. Eng.*, vol. 28, no. 8, pp. 836–848, 2000.

[33] D. R. Bell, *Cardiac Muscle Mechanics and the Cardiac Pump*. Baltimore, MD, USA: Williams & Wilkins, 2009, sec. 13, pp. 243–263.

[34] G. Gobbel and J. Fike, "A deconvolution method for evaluating indicator-dilution curves," *Phys. Med. Biol.*, vol. 39, no. 11, pp. 1833–1854, 1994.

[35] M. H. Green and J. Balmer Green, "The application of compartmental analysis to research in nutrition," *Annu. Rev. Nutrition*, vol. 10, pp. 41–61, 1990.

[36] R. R. Wolfe and D. Chinkes, *Isotope Tracer in Metabolic Research: Principles and Practice of Kinetic Analysis*, 2nd ed. Hoboken, NJ, USA: Wiley, 2005.

[37] S. P. Soubron and D. L. Buckley, "Tracer kinetic modelling in MRI: Estimating perfusion and capillary permeability," *Phys. Med. Biol.*, vol. 57, no. 2, pp. R1–R33, 2012.

[38] C. Cobelli and E. Carson, *Introduction to Modeling in Physiology and Medicine*. Amsterdam, The Netherlands: Elsevier, 2008.

[39] S. G. Sakka, R. D. A., and A. Perel, "The transpulmonary thermodilution technique," *J. Clin. Monitor*, vol. 26, pp. 347–352, 2012.

[40] D. L. H. Cheong, T. C. C. Lim, and T. S. Koh, "Dynamic contrast-enhanced CT of intracranial meningioma: Comparison of distributed and compartmental tracer kinetic models initial results," *Radiology*, vol. 232, pp. 921–930, 2004.

[41] C. Dietrich *et al.*, "An EFSUMB introduction into dynamic contrast-enhanced ultrasound (DCE-US) for quantification of tumour perfusion," *Ultraschall in der Medizin*, vol. 33, no. 4, pp. 344–351, 2012.

[42] A. Jackson, D. L. Buckley, G. J. Parker, and M. Ah-See, *Dynamic Contrast-Enhanced Magnetic Resonance Imaging in Oncology*. New York, NY, USA: Springer, 2005.

[43] J. A. Jacquez and C. P. Simon, "Qualitative theory of compartmental systems," *SIAM Rev.*, vol. 35, no. 1, pp. 43–79, 1993.

[44] G. Brix, J. Griebel, F. Kiessling, and F. Wenz, "Tracer kinetic modelling of tumour angiogenesis based on dynamic contrast-enhanced CT and MRI measurements," *Eur. J. Nucl. Med. Mol. Imag.*, vol. 37, pp. S30–S51, 2010.

[45] B. Girod, R. Rabenstein, and A. Strenger, *Signal and Systems*. New York, NY, USA: Wiley, 2001.

[46] D. Cosgrove, "Ultrasound contrast agents: An overview," *Eur. J. Radiol.*, vol. 60, no. 3, pp. 324–330, 2006.

[47] N. de Jong, P. J. Frinking, A. Bouakaz, and F. J. Ten Cate, "Detection procedures of ultrasound contrast agents," *Ultrasonics*, vol. 38, nos. 1–8, pp. 87–92, 2000.

[48] E. Quaia, "Microbubble ultrasound contrast agents: An update," *Eur. Radiol.*, vol. 17, no. 8, pp. 1995–2008, 2007.

[49] S. B. Feinstein, "The powerful microbubble: From bench to bedside, from intravascular indicator to therapeutic deliver system, and beyond," *Amer. J. Physiol-Heart C*, vol. 287, no. 2, pp. H450–H457, 2004.

[50] J. Jakobsen, R. Oyen, H. S. Thomsen, and S. K. Morcos, "Safety of ultrasound contrast agents," *Eur. Radiol.*, vol. 15, no. 5, pp. 941–945, 2005.

[51] ICUS. *Ceus around the world: Where, which agents and how they're used*. (2016). [Online]. Available: http://www.icus-society.org/attachments/article/103/ICUS_CEUS_Use_Around_the_World.pdf

[52] G. T. Haar, "Safety and bio-effects of ultrasound contrast agents," *Med. Biol. Eng. Comput.*, vol. 47, no. 8, pp. 893–900, 2009.

[53] M. L. Main *et al.*, "Acute mortality in hospitalized patients undergoing echocardiography with and without an ultrasound contrast agent (multicenter registry results in 4,300,966 consecutive patients)," *Amer. J. Cardiol.*, vol. 102, no. 12, pp. 1742–1746, 2008.

[54] F. Piscaglia and L. Bolondi, "The safety of sonovue in abdominal applications: Retrospective analysis of 23188 investigations," *Ultrasound Med. Biol.*, vol. 26, no. 6, pp. 965–975, 2000.

[55] J. Correas *et al.*, "Ultrasound contrast agents: Properties, principles of action, tolerance, and artifacts," *Eur. Radiol.*, vol. 11, no. 8, pp. 1316–1328, 2001.

[56] T. G. Leighton, *The Acoustic Bubble*. San Diego, CA, USA: Academic, 1994.

[57] P. Marmottant *et al.*, "A model for large amplitude oscillations of coated bubbles accounting for buckling and rupture," *J. Acoust. Soc. Amer.*, vol. 118, no. 6, pp. 3499–3505, 2005.

[58] M. Mischi, N. G. Rognin, and M. Averkiou, *Ultrasound Imaging Modalities*. Amsterdam, The Netherlands: Elsevier, 2014, sec. 2.15.

[59] A. Prosperetti and A. Lezzi, "Bubble dynamics in a compressible liquid. part 1. First-order theory," *J. Fluid Mech.*, vol. 168, pp. 457–478, 1986.

[60] F. Calliada, R. Campani, O. Bottinelli, A. Bozzini, and M. G. Sommaruga, "Ultrasound contrast agents: Basic principles," *Eur. J. Radiol.*, vol. 27, pp. S157–S160, 1998.

[61] A. Sodickson *et al.*, "Recurrent CT, cumulative radiation exposure, and associated radiation-induced cancer risks from CT of adults," *Radiology*, vol. 251, no. 1, pp. 175–184, 2009.

[62] M. Mischi, T. Kalker, and E. Korsten, "Videodensitometric methods for cardiac output measurements," *EURASIP J. Appl. Signal Process.*, vol. 5, pp. 479–489, 2003.

[63] N. G. Rognin, P. J. Frinking, M. Costa, and M. Arditi, "In-vivo perfusion quantification by contrast ultrasound:validation of the use of linearized video data vs. raw RF data," in *Proc. IEEE Int. Ultrasonics Symp.*, 2008, pp. 1690–1693.

[64] D. J. Collins and A. R. Padhani, "Dynamic magnetic resonance imaging of tumor perfusion. Approaches and biomedical challenges," *IEEE Eng. Med. Biol. Mag.*, vol. 23, no. 5, pp. 65–83, Sep./Oct., 2004.

[65] S. Delorme and M. Krix, "Contrast-enhanced ultrasound for examining tumor biology," *Cancer Imag.*, vol. 6, no. 1, pp. 148–152, 2006.

[66] R. García Figueiras, A. Padhani, J. Vilanova Busquets, V. Goh, and C. Villalba Martn, "Functional imaging of tumors. Part 1," *Radiologia*, vol. 52, no. 2, pp. 115–125, 2012.

[67] M. Krix, "Quantification of enhancement in contrast ultrasound: A tool for monitoring of therapies in liver metastases," *Eur. Radiol. Supplements*, vol. 15, no. Supplement 5, pp. E104–E108, 2005.

[68] C. Strouthos, M. Lampaskis, V. Sboros, A. McNeilly, and M. Averkiou, "Indicator dilution models for the quantification of microvascular blood flow with bolus administration of ultrasound contrast agents," *IEEE Trans. Ultrason. Ferrelectr. Freq. Control*, vol. 57, no. 6, pp. 1296–1310, Jun. 2010.

[69] K. W. Ferrara and C. R. Merritt, "Evaluation of tumor angiogenesis with us: Imaging, doppler, and contrast agents," *Acad. Radiol.*, vol. 7, no. 10, pp. 824–839, 2000.

[70] C. Greis, "Ultrasound contrast agents as markers of vascularity and microcirculation," *Clin. Hemorheol. Micro.*, vol. 43, no. 1, pp. 1–9, 2009.

[71] N. Lassau, L. Chami, B. Benatsou, P. Peronneau, and A. Roche, "Dynamic contrast-enhanced ultrasonography (DCE-US) with quantification of tumor perfusion: A new diagnostic tool to evaluate the early effects of antiangiogenic treatment," *Eur. Radiol. Supplements*, vol. 17, no. 6 Supplement, pp. F89–F98, 2007.

[72] M. Smeenge, M. Mischi, M. P. Laguna Pes, J. J. de la Rosette, and H. Wijkstra, "Novel contrast-enhanced ultrasound imaging in prostate cancer," *World J. Urol.*, vol. 29, no. 5, pp. 581–587, 2011.

[73] M. Wink *et al.*, "Contrast-enhanced ultrasound and prostate cancer; A multicentre european research coordination project," *Eur. Urol.*, vol. 54, no. 5, pp. 982–993, 2008.

[74] M. Mischi, T. A. Kalker, and E. H. Korsten, "Contrast echocardiography for pulmonary blood volume quantification," *IEEE Trans. Ultrason. Ferrelectr. Freq. Control*, vol. 51, no. 9, pp. 1137–1147, Sep. 2004.

[75] M. Arditi and P. J. A. Frinking, "A new formalism for the quantification of tissue perfusion by the destruction-replenishment method in contrast ultrasound imaging," *IEEE Trans. Ultrason. Ferrelectr. Freq. Control*, vol. 53, no. 6, pp. 1118–1129, Jun. 2006.

[76] J. M. Hudson, R. Karshafian, and P. N. Burns, "Quantification of flow using ultrasound and microbubbles: A disruption replenishment model based on physical principles," *Ultrasound Med. Biol.*, vol. 35, no. 12, pp. 2007–2020, 2009.

[77] K. Wei *et al.*, "Quantification of myocardial blood flow with ultrasound-induced destruction of microbubbles administered as a constant venous infusion," *Circulation*, vol. 97, pp. 473–483, 1998.

[78] P. Meier and K. Zierler, "On the theory of the indicator-dilution method for measurement of blood flow and volume," *J. Appl. Physiol.*, vol. 6, pp. 731–744, 1954.

[79] M. P. J. Kuenen, M. Mischi, and H. Wijkstra, "Contrast-ultrasound diffusion imaging for localization of prostate cancer," *IEEE Trans. Med. Imag.*, vol. 30, no. 8, pp. 1493–1502, Aug. 2011.

[80] M. Lampaskis and M. Averkiou, "Investigation of the relationship of nonlinear backscattered ultrasound intensity with microbubble concentration at low MI," *Ultrasound Med. Biol.*, vol. 36, no. 2, pp. 306–312, 2010.

[81] K. Zierler, "Theoretical basis of indicator-dilution methods for measuring flow and volume," *Circulation Res.*, vol. 10, no. 3, pp. 393–407, 1962.

[82] D. M. Band, R. A. Linton, T. K. O'Brien, M. M. Jonas, and N. W. Linton, "The shape of indicator dilution curves used for cardiac output measurement in man," *J. Physiology*, vol. 498, no. 1, pp. 225–229, 1997.

[83] H. Qian and J. B. Bassingthwaighte, "A class of flow bifurcation models with lognormal distribution and fractal dispersion," *J. Theor. Biol.*, vol. 205, no. 2, pp. 261–268, 2000.

[84] J. Brands, H. Vink, and J. W. G. E. Van Teeffelen, "Comparison of four mathematical models to analyze indicator-dilution curves in the coronary circulation," *Med. Biol. Eng. Comput.*, vol. 49, no. 12, pp. 1471–1479, 2011.

[85] R. Davenport, "The derivation of the gamma-variate relationship for tracer dilution curves," *J. Nucl. Med.*, vol. 24, no. 10, pp. 945–948, 1983.

[86] M. Mischi, J. Den Boer, and H. Korsten, "On the physical and stochastic representation of an indicator dilution curve as a gamma variate," *Physiol. Meas.*, vol. 29, no. 3, pp. 281–294, 2008.

[87] E. Leonard and S. B. Jorgensen, "The analysis of convection and diffusion in capillary beds," *Annu. Rev. Biophys. Bio.*, vol. 3, no. 293–339, 1974.

[88] G. Taylor, "Dispersion of soluble matter in solvent flowing slowly through a tube," *Proc. Roy. Soc. London A*, vol. 219, no. 1137, pp. 186–203, 1953.

[89] M. D. Harpen and M. L. Lecklitner, "Derivation of gamma variate indicator dilution function from simple convective dispersion model of blood flow," *Med. Phys.*, vol. 11, no. 5, pp. 690–692, 1984.

[90] J. M. Bogaard, S. J. Smith, A. Versprille, M. E. Wise, and F. Hagemeijer, "Physiological interpretation of the skewness of indicator dilution curves; theoretical considerations and a practical application," *Basic Res. Cardiol.*, vol. 79, no. 4, pp. 479–493, 1984.

[91] J. M. Bogaard, J. R. C. Jansen, E. A. von Reth, A. Versprille, and M. E. Wise, "Random walk types models for indicator-dilution studies: Comparison of a local density random walk and a first passage times distribution," *Cardiovasc. Res.*, vol. 20, no. 11, pp. 789–796, 1986.

[92] R. K. Millard, "Indicator-dilution dispersion models and cardiac output computing methods," *Amer. J. Physiol. Heart Circ. Physiol.*, vol. 272, no. 4, pp. H2004–H2012, 1997.

[93] K. Norwich and S. Zelin, "The dispersion of indicator in the cardiopulmonary system," *Bull. Math. Biophys.*, vol. 32, no. 1, pp. 25–43, 1970.

[94] E. A. von Reth and J. M. Boogard, "Comparison of a two-compartment model and distributed models for indicator dilution studies," *Med. Biol. Eng. Comput.*, vol. 21, pp. 453–459, 1983.

[95] C. W. Sheppard and L. J. Savage, "The random walk problem in relation to the physiology of circulatory mixing," *Phys. Rev.*, vol. 83, no. 2, pp. 489–490, 1951.

[96] A. Papoulis, *Probability, Random Variables, and Stochastic Processes*. New York, NY, USA: McGraw-Hill, 1965.

[97] M. E. Wise, "Tracer dilution curves in cardiology and random walk and lognormal distributions," *Acta Phyisiologica et Pharamcologica Neerlandica*, vol. 14, pp. 175–204, 1966.

[98] J. B. Bassingrhwaighre, F. H. Ackerman, and E. H. Wood, "Applications of the lagged normal density curve as a model for arterial dilution curves," *Circulation Res.*, vol. 18, no. 4, pp. 398–415, 1966.

[99] J. Davis, C. Guy, and M. H. Kutner, "The lagged normal family of probability density functions applied to indicator-dilution curves," *Biometrics*, vol. 32, no. 3, pp. 669–675, 1976.

[100] M. Krix *et al.*, "A multivessel model describing replenishment kinetics of ultrasound contrast agent for quantification of tissue perfusion," *Ultrasound Med. Biol.*, vol. 29, no. 10, pp. 669–675, 2003.

[101] C. Greis, "Quantitative evaluation of microvascular blood flow by contrast-enhanced ultrasound (CEUS)," *Clin. Hemorheol. Micro.*, vol. 49, pp. 137–149, 2011.

[102] O. Lucidarme *et al.*, "Blood flow quantification with contrast-enhanced US: "Entrance in the section" phenomenon–phantom and rabbit study," *Radiology*, vol. 228, pp. 473–479, 2003.

[103] T. C. Potdevin, J. B. Fowlkes, A. P. Moskalik, and P. L. Carson, "Analysis of refill curve shape in ultrasound contrast agent studies," *Med. Phys.*, vol. 31, no. 3, pp. 623–632, 2004.

[104] J. M. Hudson *et al.*, "Improved flow measurement using microbubble contrast agents and disruption-replenishment: Clinical application to tumour monitoring," *Ultrasound Med. Biol.*, vol. 37, no. 8, pp. 1210–1221, 2011.

[105] V. Goh and A. R. Padhani, "Imaging tumor angiogenesis: functional assessment using MDCT or MRI?" *Abdominal Imag.*, vol. 31, no. 2, pp. 194–199, 2006.

[106] R. Karshafian, P. N. Burns, and M. R. Henkelman, "Transit time kinetics in ordered and disordered vascular trees," *Phys. Med. Biol.*, vol. 48, no. 19, pp. 3225–3237, 2003.

[107] M. Kuenen, T. Saidov, H. Wijkstra, and M. Mischi, "Contrast-ultrasound dispersion imaging for prostate cancer localization by improved spatiotemporal similarity analysis," *Ultrasound Med. Biol.*, vol. 39, no. 9, pp. 1631–1641, 2013.

[108] M. Mischi, Z. Del Prete, and H. Korsten, *Indicator Dilution Techniques in Cardiovascular Quantification*. Singapore: World Scientific Publishing, 2007, sec. 4, pp. 89–155.

[109] G. V. Strijkers, W. J. Mulder, G. A. van Tilborg, and K. Nicolay, "MRI contrast agents: Current status and future perspectives," *Anti-Cancer Agent Med. Chem.*, vol. 7, no. 3, pp. 291–305, 2007.

[110] M. Mischi and J. A. Blom, *Flow Sensor for Liquids*. New York, NY, USA: Monument Press, 2010, sec. 2, pp. 89–91.

[111] M. F. Bellin and A. J. Van Der Molen, "Extracellular gadolinium-based contrast media: An overview," *Eur. J. Radiol.*, vol. 66, no. 2, pp. 160–167, 2008.

[112] T. P. L. Roberts and M. D. Noseworthy, *Contrast Agents for Magnetic Resonance Imaging*. New York, NY, USA: Springer, 2003, sec. 2, pp. 23–37.

[113] A. R. Padhani, "Dynamic contrast-enhanced MRI in clinical oncology: Current status and future directions," *J. Magn. Resonance Imag.*, vol. 16, pp. 407–422, 2002.

[114] D. L. Buckley and G. J. Parker, *Measuring Contrast Agent Concentration in T1-Weighted Dynamic Contrast-Enhanced MRI*. New York, NY, USA: Springer, 2003, sec. 5, pp. 69–79.

[115] R. C. Brasch and C. Li, King, "In-vivo monitoring of tumor angiogenesis with MR imaging," *Acad. Radiol.*, vol. 7, no. 10, pp. 812–23, 2000.

[116] C. Preibisch and R. Deichmann, "Influence of RF spoiling on the stability and accuracy of T1 mapping based on spoiled FLASH with varying flip angles," *Magn. Reson. Med.*, vol. 61, no. 1, pp. 125–135, 2009.

[117] G. J. Parker *et al.*, "Probing tumor microvascularity by measurement, analysis and display of contrast agent uptake kinetics," *J. Magn. Resonance Imag.*, vol. 7, no. 3, pp. 564–574, 1997.

[118] P. S. Tofts, B. Berkowitz, and M. D. Schnall, "Quantitative analysis of dynamic Gd-DTPA enhancement in breast tumors using a permeability model," *Magn. Resonance Med.*, vol. 33, pp. 564–568, 1995.

[119] J. Pintaske *et al.*, "Relaxivity of gadopentetate dimeglumine (magnevist), gadobutrol (gadovist), and gadobenate dimeglumine (multihance) in human blood plasma at 0.2, 1.5, and 3 Tesla," *Invest. Radiol.*, vol. 41, no. 3, pp. 213–221, 2006.

[120] H. M. Cheng and G. A. Wright, "Rapid highesolution T1 mapping by variable flip angles: Accurate and precise measurements in the presence of radiofrequency field inhomogeneity," *Magn. Resonance Med.*, vol. 55, no. 3, pp. 566–574, 2006.

[121] I. L. Pykett, B. R. Rosen, F. S. Buonanno, and T. J. Brady, "Measurement of spin-lattice relaxation times in nuclear magnetic resonance imaging," *Phys. Med. Biol.*, vol. 28, no. 6, pp. 723–729, 1983.

[122] L. J. Bains *et al.*, "Tracer kinetic analysis of dynamic contrast-enhanced MRI and CT bladder cancer data: A preliminary comparison to assess the magnitude of water exchange effects," *Magn. Resonance Med.*, vol. 64, pp. 595–603, 2010.

[123] E. M. Renkin, "Transport of potassium-42 from blood to tissue in isolated mammalian skeletal muscles," *Amer. J. Physiol.*, vol. 197, pp. 1205–1210, 1959.

[124] K. L. Zierler, "Equations for measuring blood flow by external monitoring of radioisotopes," *Circulation Res.*, vol. 16, no. 4, pp. 309–321, 1965.

[125] K. S. S. Lawrence and T.-Y. Lee, "An adiabatic approximation to the tissue homogeneity model for water exchange in the brain: I. theoretical derivation," *J. Cerebrial Blood Flow Metabol.*, vol. 18, no. 12, pp. 1365–1377, 1998.

[126] M. R. Orton *et al.*, "Computationally efficient vascular input function models for quantitative kinetic modelling using CT," *Phys. Med. Biol.*, vol. 53, no. 5, pp. 1225–1239, 2008.

[127] P. S. Tofts and A. G. Kermode, "Measurement of the blood-brain barrier permeability and leakage space using dynamic MR imaging. 1. Fundamental concepts," *Magn. Resonance Med.*, vol. 17, no. 2, pp. 357–367, 1991.

[128] M. Ingrisch and S. Sourbron, "Tracer-kinetic modeling of dynamic contrast-enhanced MRI and CT: A primer," *J. Pharmacokinet Pharmacodyn*, vol. 40, no. 3, pp. 281–300, 2013.

[129] G. J. M. Parker *et al.*, "Experimentally-derived functional form for a population-averaged high-temporal-resolution arterial input function for dynamic contrast-enhanced MRI," *Magn. Resonance Med.*, vol. 56, no. 5, pp. 993–1000, 2006.

[130] T. E. Yankeelov *et al.*, "Quantitative pharmacokinetic analysis of CT data without an arterial input function: A reference region model," *Magn. Resonance Imag.*, vol. 23, no. 4, pp. 519–529, 2005. [Online]. Available: http://www.sciencedirect.com/science/article/pii/S0730725X05001359

[131] T. S. Koh, L. H. Cheong, Z. Hou, and Y. C. Soh, "A physiologic model of capillary-tissue exchange for dynamic contrast-enhanced imaging of tumor microcirculation," *IEEE Trans. Bio-Med. Eng.*, vol. 50, no. 2, pp. 159–167, Feb. 2003.

[132] S. P. Sourbron and D. L. Buckley, "On the scope and interpretation of the Tofts models for CT," *Magn. Resonance Med.*, vol. 66, no. 3, pp. 735–745, 2011.

[133] S. P. Sourbron and D. L. Buckley, "Classic models for dynamic contrast-enhanced MRI," *NMR Biomed.*, vol. 26, no. 8, pp. 1004–1027, 2013.

[134] J. A. Johnson and T. A. Wilson, "A model for capillary exchange," *Amer. J. Physiol.*, vol. 210, pp. 299–1303, 1966.

[135] Y. Sawada, C. S. Patlak, and R. G. Blasberg, "Kinetic analysis of cerebrovascular transport based on indicator diffusion technique," *Amer. J. Physiol.*, vol. 256, no. 3, pp. H794–H812, 1989.

[136] L. E. Kershaw and D. L. Buckley, "Precision in measurements of perfusion and microvascular permeability with T1-weighted dynamic contrast-enhanced MRI," *Magn. Resonance Med.*, vol. 56, no. 5, pp. 986–992, 2006.

[137] M. F. Morales and R. E. Smith, "On the theory of blood-tissue exchange of inert gases: VI. validity of approximate uptake expressions," *Bull. Math. Biophys.*, vol. 10, no. 3, pp. 191–200, 1948.

[138] S. S. Kety, "The theory and applications of the exchange of inert gas at the lungs and tissues," *Pharmacol. Rev.*, vol. 3, no. 1, pp. 1–41, 1951.

[139] G. Brix, M. L. Bahner, U. Hoffmann, A. Horvath, and W. Schreiber, "Regional blood flow, capillary permeability, and compartmental volumes: Measurement with dynamic CT - initial experience," *Radiology*, vol. 210, no. 1, pp. 269–276, 1999.

[140] G. Brix *et al.*, "Microcirculation and microvasculature in breast tumors: Pharmacokinetic analysis of dynamic MR image series," *Magn. Resonance Med.*, vol. 52, no. 2, pp. 420–429, 2004.

[141] S. B. Donaldson *et al.*, "A comparison of tracer kinetic models for T1-weighted dynamic contrast-enhanced MRI: Application in carcinoma of the cervix," *Magn. Resonance Med.*, vol. 63, no. 3, pp. 691–700, 2010.

[142] L. E. Kershaw and H. M. Cheng, "Temporal resolution and SNR requirements for accurate DCE-MRI data analysis using the AATH model," *Magn. Resonance Med.*, vol. 64, no. 6, pp. 1772–1780, 2010.

[143] R. Luypaert, S. Sourbron, S. Makkat, and J. D. Mey, "Error estimation for perfusion parameters obtained using the two-compartment exchange model in dynamic contrast-enhanced MRI: A simulation study," *Phys. Med. Biol.*, vol. 55, no. 21, pp. 6431–6443, 2010.

[144] J. H. Naish *et al.*, "Modeling of contrast agent kinetics in the lung using T1-weighted dynamic contrast-enhanced MRI," *Magn. Resonance Med.*, vol. 61, no. 6, pp. 1507–1514, 2009.

[145] P. S. Tofts, "Modeling tracer kinetics in dynamic Gd-DTPA mr imaging," *J. Magn. Resonance Imag.*, vol. 7, no. 1, pp. 91–101, 1997.

[146] H. B. Larsson *et al.*, "Quantitation of blood-brain barrier defect by magnetic resonance imaging and gadolinium-DTPA in patients with multiple sclerosis and brain tumors," *Magn. Resonance Med.*, vol. 16, no. 1, pp. 117–131, 1990.

[147] G. Brix *et al.*, "Pharmacokinetic parameters in CNS Gd-DTPA enhanced MR imaging," *J. Comput. Assisted Tomography*, vol. 15, no. 4, pp. 621–628, 1991.

[148] P. S. Tofts *et al.*, "Estimating kinetic parameters from dynamic contrast-enhanced T1-weighted MRI of a diffusable tracer: Standardized quantities and symbols," *J. Magn. Resonance Imag.*, vol. 10, no. 3, pp. 223–232, 1999.

[149] P. L. Choyke, A. J. Dwyer, and M. V. Knopp, "Functional tumor imaging with dynamic contrast-enhanced magnetic resonance imaging," *J. Magn. Resonance Imag.*, vol. 17, no. 5, pp. 509–520, 2003.

[150] Q. G. de Lussanet *et al.*, "Dynamic contrast-enhanced MRI of muscle perfusion combined with MR angiography of collateral artery growth in a femoral artery ligation model," *NMR Biomed.*, vol. 20, no. 8, pp. 717–725, 2007.

[151] C. Hayes, A. R. Padhani, and M. O. Leach, "Assessing changes in tumour vascular function using dynamic contrast-enhanced magnetic resonance imaging," *NMR Biomed.*, vol. 15, no. 2, pp. 154–163, 2002.

[152] M. Leach, "Breast imaging technology: Application of magnetic resonance imaging to angiogenesis in breast cancer," *Breast Cancer Res.*, vol. 3, no. 1, pp. 22–27, 2001.

[153] N. A. Pack and E. V. R. Di Bella, "Comparison of myocardial perfusion estimates from dynamic contrast-enhanced magnetic resonance imaging with four quantitative analysis methods," *Magn. Resonance Med.*, vol. 64, no. 1, pp. 125–137, 2010.

[154] C. S. Patlak, R. G. Blasberg, and J. D. Fenstermacher, "Graphical evaluation of blood-to-brain transfer constants from multiple-time uptake data," *J. Cerebral Blood Flow Metabolism*, vol. 3, no. 1, pp. 1–7, 1983.

[155] S. Sourbron, M. Ingrisch, A. Siefert, M. Reiser, and K. Herrmann, "Quantification of cerebral blood flow, cerebral blood volume, and blood brain-barrier leakage with CT," *Magn. Resonances Med.*, vol. 62, no. 1, pp. 205–217, 2009.

[156] C. S. Patlak and R. G. Blasberg, "Graphical evaluation of blood-to-brain transfer constants from multiple-time uptake data. generalizations," *J. Cerebral Blood Flow Metabolism*, vol. 5, no. 4, pp. 584–590, 1985.

[157] F. Calamante, D. G. Gadian, and A. Connelly, "Delay and dispersion effects in dynamic susceptibility contrast MRI: Simulations using singular value decomposition," *Magn. Resonance Med.*, vol. 44, no. 3, pp. 466–473, 2000.

[158] F. Calamante, P. J. Yim, and J. R. Cebral, "Estimation of bolus dispersion effects in perfusion MRI using image-based computational fluid dynamics," *NeuroImage*, vol. 19, no. 2, pp. 341–353, 2003.

[159] L. Ko, M. Salluzzi, R. Frayne, and M. Smith, "Reexamining the quantification of perfusion MRI data in the presence of bolus dispersion," *J. Magn. Resonance Imag.*, vol. 25, no. 3, pp. 639–643, 2007.

[160] M. J. P. van Osch, J. van der Grond, and C. J. G. Bakker, "Partial volume effects on arterial input functions: Shape and amplitude distortions and their correction," *J. Magn. Resonance Imag.*, vol. 22, no. 6, pp. 704–709, 2005.

[161] F. Peeters, L. Annet, L. Hermoye, and B. E. Van Beers, "Inflow correction of hepatic perfusion measurements using T1-weighted, fast gradient-echo, contrast-enhanced MRI," *Magn. Resonance Med.*, vol. 51, no. 4, pp. 710–717, 2004.

[162] C. Roberts *et al.*, "The effect of blood inflow and B1-field inhomogeneity on measurement of the arterial input function in axial 3D spoiled gradient echo dynamic contrast-enhanced MRI," *Magn. Resonance Med.*, vol. 65, no. 1, pp. 108–119, 2011.

[163] L. E. Kershaw and H.-L. M. Cheng, "A general dual-bolus approach for quantitative CT," *Magn. Resonance Imag.*, vol. 29, no. 2, pp. 160–166, 2011.

[164] M. Mischi *et al.*, "Magnetic resonance dispersion imaging for localization of angiogenesis and cancer growth," *Investigative Radiol.*, vol. 49, no. 8, pp. 561–569, 2014.

[165] B. R. Rosen, J. W. Belliveau, J. M. Vevea, and T. J. Brady, "Perfusion imaging with NMR contrast agents," *Magn. Resonance Med.*, vol. 14, no. 2, pp. 249–265, 1990.

[166] R. A. Lindenet *et al.*, "Contrast enhanced ultrasound flash replenishment method for directed prostate biopsies," *J. Urology*, vol. 178, no. 6, pp. 2354–2358, 2007.

[167] J. J. Fütterer *et al.*, "Prostate cancer localization with dynamic contrast-enhanced MR imaging and proton MR spectroscopic imaging," *Radiology*, vol. 241, no. 2, pp. 449–458, 2006.

[168] C. M. A. Hoeks *et al.*, "Prostate cancer: Multiparametric MR imaging for detection, localization, and staging," *Radiology*, vol. 261, no. 1, pp. 46–66, 2011.

[169] T. Albrecht *et al.*, "Improved detection of hepatic metastases with pulse-inversion US during the liver-specific phase of SHU 508A: Multicenter study," *Radiology*, vol. 227, no. 2, pp. 361–370, 2003.

[170] R. Konopke, A. Bunk, and S. Kersting, "The role of contrast-enhanced ultrasound for focal liver lesion detection: An overview," *Ultrasound Med. Biol.*, vol. 33, no. 10, pp. 1515–1526, 2007.

[171] A. Heidenreich *et al.*, "EAU guidelines on prostate cancer. part 1: Screening, diagnosis, and treatment of clinically localised disease," *Eur. Urol.*, vol. 59, no. 1, pp. 61–71, 2011.

[172] F. Piscaglia *et al.*, "Characterization of focal liver lesions with contrast-enhanced ultrasound," *Ultrasound Med. Biol.*, vol. 36, no. 4, pp. 531–550, 2010.

[173] T. D'Arcy *et al.*, "Ovarian cancer detected non-invasively by contrast-enhanced power doppler ultrasound," *BJOG*, vol. 111, no. 6, pp. 619–622, 2004.

[174] J. Wang *et al.*, "Study on the characteristics of contrast-enhanced ultrasound and its utility in assessing the microvessel density in ovarian tumors or tumor-like lesions," *Int. J. Biol. Sci.*, vol. 7, no. 5, pp. 600–606, 2011.

[175] C. Wan, J. Du, H. Fang, F. Li, and L. Wang, "Evaluation of breast lesions by contrast enhanced ultrasound: Qualitative and quantitative analysis," *Eur. J. Radiol.*, vol. 81, no. 4, pp. e444–e450, 2011.

[176] M. Chaudhari *et al.*, "Breast tumor vascularity identified by contrast enhanced ultrasound and pathology: Initial results," *Ultrasonics*, vol. 38, nos. 1–8, pp. 105–109, 2000.

[177] H. Zhao *et al.*, "Contrast-enhanced ultrasound is helpful in the differentiation of malignant and benign breast lesions," *Eur. J. Radiol.*, vol. 73, no. 2, pp. 288–293, 2010.

[178] H. Tamai *et al.*, "Contrast-enhanced ultrasonography in the diagnosis of solid renal tumors," *J. Ultrasound Med.*, vol. 24, no. 12, pp. 1635–1640, 2005.

[179] S. R. Wilson and P. N. Burns, "Microbubble-enhanced US in body imaging: What role?" *Radiology*, vol. 257, no. 1, pp. 24–39, 2010.

[180] Z. Fan *et al.*, "Application of contrast-enhanced ultrasound in the diagnosis of solid pancreatic lesion: A comparison of conventional ultrasound and contrast-enhanced CT," *Eur. J. Radiol.*, vol. 92, no. 9, pp. 1385–1390, 2013.

[181] M. Wink, J. de la Rosette, C. Grimbergen, and H. Wijkstra, "Transrectal contrast enhanced ultrasound for diagnosis of prostate cancer," *World J. Urol*, vol. 25, no. 4, pp. 367–373, 2007.

[182] G. Xu *et al.*, "Parameters of prostate cancer at contrast-enhanced ultrasound: Correlation with prostate cancer risk," *Int. J. Clin. Exp. Med.*, vol. 8, no. 2, pp. 2562–2569, 2015.

[183] T. Ichikawa *et al.*, "Detection and characterization of focal liver lesions: A japanese phase III, multicenter comparison between gadoxetic acid disodium-enhanced magnetic resonance imaging and contrast-enhanced computed tomography predominantly in patients with hepatocellular carcinoma and chronic liver disease," *Investigative Radiol.*, vol. 45, no. 3, pp. 133–141, 2010.

[184] S. H. Kim, A. Kamaya, and J. K. Willmann, "CT perfusion of the liver: Principles and applications in oncology," *Radiology*, vol. 272, no. 2, pp. 322–344, 2014.

[185] G. Barrois, A. Coron, T. Payen, A. Dizeux, and L. Bridal, "A multiplicative model for improving microvascular flow estimation in dynamic contrast-enhanced ultrasound (DCE-US): Theory and experimental validation," *IEEE Trans. Ultrason. Ferroeletr. Freq. Control*, vol. 60, no. 11, pp. 2284–2294, Nov. 2013.

[186] J. F. Schaefer *et al.*, "Solitary pulmonary nodules: Association between signal characteristics in dynamic contrast enhanced MRI and tumor angiogenesis," *Lung Cancer*, vol. 53, no. 1, pp. 39–49, 2006.

[187] M. A. Bali *et al.*, "Tumoral and nontumoral pancreas: Correlation between quantitative dynamic contrast-enhanced MR imaging and histopathologic parameters," *Radiology*, vol. 261, no. 2, pp. 456–466, 2011.

[188] J. H. Kim *et al.*, "Solid pancreatic lesions: Characterization by using timing bolus dynamic contrast-enhanced MR imaging assessment—A preliminary study," *Radiology*, vol. 266, no. 1, pp. 185–196, 2013.

[189] H. Hawighorst *et al.*, "Angiogenic activity of cervical carcinoma: Assessment by functional magnetic resonance imaging-based parameters and a histomorphological approach in correlation with disease outcome," *Clin. Cancer Res.*, vol. 4, no. 10, pp. 2305–2312, 1998.

[190] F. Kar-Ho Lee, A. D. King, B. Buig-Yue Ma, and D. Ka-wai Yeung, "Dynamic contrast enhancement magnetic resonance imaging (CT) for differential diagnosis in head and neck cancers," *Eur. J. Radiol.*, vol. 81, no. 4, pp. 784–788, 2012.

[191] M. Notohamiprodjo, "Measuring perfusion and permeability in renal cell carcinoma with dynamic contrast-enhanced MRI: A pilot study," *J. Magn. Resonance Imag.*, vol. 31, no. 2, pp. 490–501, 2010.

[192] S. U. Aswathy, G. G. D. Dhas, and S. S. Kumar, "A survey on detection of brain tumor from MRI brain images," in *Proc. Int. Conf. Control, Instrum. Commun. Comput. Technol.*, 2014, pp. 871–877.

[193] T. Franiel *et al.*, "Evaluation of normal prostate tissue, chronic prostatitis, and prostate cancer by quantitative perfusion analysis using a dynamic contrast-enhanced inversion-prepared dual-contrast gradient echo sequence," *Investigative Radiol.*, vol. 43, no. 7, pp. 481–487, 2008.

[194] A. S. N. Jackson *et al.*, "Dynamic contrast-enhanced MRI for prostate cancer localization," *Brit. J. Radiol.*, vol. 82, no. 974, pp. 148–156, 2009.

[195] X. Fan *et al.*, "Diagnosis of suspicious breast lesions using an empirical mathematical model for dynamic contrast-enhanced MRI," *Magn. Resonance Imag.*, vol. 25, no. 5, pp. 593–603, 2007.

[196] E. Furman-Haran, E. Schechtman, F. Kelcz, K. Kirshenbaum, and H. Degani, "Magnetic resonance imaging reveals functional diversity of the vasculature in benign and malignant breast lesions," *Cancer*, vol. 104, no. 4, pp. 708–718, 2005.

[197] R. García-Figueiras *et al.*, "CT perfusion in oncologic imaging: A useful tool?" *Amer. J. Roentgenol.*, vol. 200, no. 1, pp. 8–19, 2013.

[198] V. Goh *et al.*, "Differentiation between diverticulitis and colorectal cancer: Quantitative CT perfusion measurements versus morphologic criteria initial experience 1," *Radiology*, vol. 242, no. 2, pp. 456–462, 2007.

[199] C. S. Reiner *et al.*, "Computed tomography perfusion imaging of renal cell carcinoma: systematic comparison with histopathological angiogenic and prognostic markers," *Investigative Radiol.*, vol. 48, no. 4, pp. 183–191, 2013.

[200] D. Ippolito, C. Capraro, A. Casiraghi, C. Cestari, and S. Sironi, "Quantitative assessment of tumour associated neovascularisation in patients with liver cirrhosis and hepatocellular carcinoma: Role of dynamic-CT perfusion imaging," *Eur. Radiol.*, vol. 22, no. 4, pp. 803–811, 2012.

[201] C. J. Diederich, "Thermal ablation and high-temperature thermal therapy: Overview of technology and clinical implementation," *Int. J. Hyperthermia*, vol. 21, no. 8, pp. 745–753, 2005.

[202] G. S. Gazelle, S. N. Goldberg, L. Solbiati, and T. Livraghi, "Tumor ablation with radio-frequency energy," *Radiology*, vol. 217, no. 3, pp. 633–646, 2000.

[203] J. E. Kennedy, "High-intensity focused ultrasound in the treatment of solid tumours," *Nat. Rev. Cancer*, vol. 5, no. 4, pp. 321–327, 2005, 10.1038/nrc1591.

[204] S. E. Eggener *et al.*, "Focal therapy for localized prostate cancer: A critical appraisal of rationale and modalities," *J. Urol.*, vol. 178, no. 6, pp. 2260–2267, 2007.

[205] C. Månsson *et al.*, "Safety and preliminary efficacy of ultrasound-guided percutaneous irreversible electroporation for treatment of localized pancreatic cancer," *Anticancer Res.*, vol. 34, no. 1, pp. 289–293, 2014.

[206] H. U. Ahmed, C. Moore, and M. Emberton, "Minimally-invasive technologies in uro-oncology: The role of cryotherapy, HIFU and photodynamic therapy in whole gland and focal therapy of localised prostate cancer," *Surg. Oncol.*, vol. 18, no. 3, pp. 219–232, 2009.

[207] J. S. Lewin *et al.*, "Interactive MRI-guided radiofrequency interstitial thermal ablation of abdominal tumors: Clinical trial for evaluation of safety and feasibility," *J. Magn. Resonance Imag.*, vol. 8, no. 1, pp. 40–47, 1998.

[208] S. Eggener *et al.*, "Focal therapy for prostate cancer: Possibilities and limitations," *Eur. Urol.*, vol. 58, no. 1, pp. 57–64, 2010.

[209] P. J. Kneeshaw, L. W. Turnbull, A. Smith, and P. J. Drew, "Dynamic contrast enhanced magnetic resonance imaging aids the surgical management of invasive lobular breast cancer," *Eur. J. Surg. Oncol.*, vol. 29, no. 1, pp. 32–37, 2003.

[210] B. G. Muller *et al.*, "The role of magnetic resonance imaging (MRI) in focal therapy for prostate cancer: Recommendations from a consensus panel," *BJU Int.*, vol. 113, no. 2, pp. 218–227, 2014.

[211] S. N. Goldberg, G. S. Gazelle, and P. R. Mueller, "Thermal ablation therapy for focal malignancy," *Amer. J. Roentgenol.*, vol. 174, no. 2, pp. 323–331, 2000.

[212] F. Knieling *et al.*, "Early response to anti-tumoral treatment in hepatocellular carcinoma—Can quantitative contrast-enhanced ultrasound predict outcome?" *Ultraschall in der Medizin*, vol. 34, no. 1, pp. 38–46, 2012.

[213] M. Lamuraglia *et al.*, "Clinical relevance of contrast-enhanced ultrasound in monitoring anti-angiogenic therapy of cancer: Current status and perspectives," *Critical Rev. Oncol.-Hemetol.*, vol. 73, no. 3, pp. 202–121, 2010.

[214] E. Quaia, "Assessment of tissue perfusion by contrast-enhanced ultrasound," *Eur. Radiol.*, vol. 21, no. 3, pp. 604–615, 2011.

[215] M. Braunagel, A. Graser, M. F. Reiser, and M. Notohamiprodjo, "The role of functional imaging in the era of targeted therapy of renal cell carcinoma," *World J. Urol.*, vol. 32, pp. 47–58, 2013.

[216] M. Lamuraglia *et al.*, "To predict progression-free survival and overall survival in metastatic renal cancer treated with sorafenib: Pilot study using dynamic contrast-enhanced doppler ultrasound," *Eur. J. Cancer*, vol. 42, no. 15, pp. 2472–2479, 2006.

[217] N. Lassau *et al.*, "Metastatic renal cell carcinoma treated with Sunitinib: Early evaluation of treatment response using dynamic contrast-enhanced ultrasonography," *Clin. Cancer Res.*, vol. 16, no. 4, pp. 1216–1225, 2010.

[218] N. Lassau *et al.*, "Gastrointestinal stromal tumors treated with Imatinib: Monitoring response with contrast-enhanced sonography," *Amer. J. Roentgenol.*, vol. 187, no. 5, pp. 1267–1273, 2006.

[219] R. Williams *et al.*, "Dynamic microbubble contrast-enhanced US to measure tumor response to targeted therapy: A proposed clinical protocol with results from renal cell carcinoma patients receiving antiangiogenic therapy," *Radiology*, vol. 260, no. 2, pp. 581–590, 2011.

[220] J. P. B. O'Connor, A. Jackson, G. J. M. Parker, and G. C. Jayson, "CT biomarkers in the clinical evaluation of antiangiogenic and vascular disrupting agents," *Brit. J. Cancer.*, vol. 96, no. 2, pp. 189–195, 2007.

[221] J. P. O'Connoar and G. C. Jayson, "Do imaging biomarkers relate to outcome in patients treated with VEGF inhibitors?" *Clin. Cancer Res.*, vol. 18, no. 24, pp. 6588–6598, 2012.

[222] L. Fournier *et al.*, "Dynamic contrast-enhanced CT (DCE-CT) as an early biomarker of response in metastatic renal cell carcinoma (mRCC) under anti-angiogenic treatment," in *Proc. ASCO Annu. Meeting*, 2007, vol. 25, p. 14003.

[223] N. Tacelli *et al.*, "Perfusion CT allows prediction of therapy response in non-small cell lung cancer treated with conventional and anti-angiogenic chemotherapy," *Eur. Radiol.*, vol. 23, no. 8, pp. 2127–2136, 2013.

[224] P. S. Murphy, T. J. McCarthy, and A. S. Dzik-Jurasz, "The role of clinical imaging in oncological drug development," *Brit. J. Radiol.*, vol. 81, no. 969, pp. 685–692, 2008.

[225] S. M. Galbraith, "Antivascular cancer treatments: Imaging biomarkers in pharmaceutical drug development," *Brit. J. Radiol.*, vol. 76 Spec no. 1, pp. S83–S86, 2003.

[226] Y. Zhu, Y. Chen, J. Jiang, R. Wang, Y. Zhou, and H. Zhang, "Contrast-enhanced harmonic ultrasonography for the assessment of prostate cancer aggressiveness: a preliminary study," *Korean J. Radiol.*, vol. 11, no. 1, pp. 75–83, 2009.

[227] V. Lazar *et al.*, "Sorafenib plus dacarbazine in solid tumors: A phase I study with dynamic contrast-enhanced ultrasonography and genomic analysis of sequential tumor biopsy samples," *Investigational New Drug*, vol. 32, no. 2, pp. 312–322, 2014.

[228] M. R. Meijerink *et al.*, "The use of perfusion CT for the evaluation of therapy combining AZD2171 with gefitinib in cancer patients," *Eur. Radiol.*, vol. 17, no. 7, pp. 1700–1713, 2007.

[229] H. Vratislav, K. Radim, M. Martin, and J. Radovan, "Comparison and evaluation of indicator dilution models for bolus of ultrasound contrast agents," *Physiol. Meas.*, vol. 34, no. 2, pp. 151–162, 2013.

[230] S. Turco *et al.*, "Time-efficient estimation of the magnetic resonance dispersion model parameters for quantitative assessment of angiogenesis," *Biomed. Signal Process.*, vol. 26, pp. 23–33, 2016.

[231] E. Henderson, B. K. Rutt, and T. Y. Lee, "Temporal sampling requirements for the tracer kinetics modeling of breast disease," *Magn Resonance Imag.*, vol. 16, no. 9, pp. 1057–1073, 1998.

[232] H.-L. Cheng, "Investigation and optimization of parameter accuracy in dynamic contrast-enhanced MRI," *J. Magn. Resonance Imag.*, vol. 28, no. 3, pp. 736–743, 2008.

[233] J. G. Korporaal, M. van Vulpen, C. A. van den Berg, and U. A. van der Heide, "Tracer kinetic model selection for dynamic contrast-enhanced computed tomography imaging of prostate cancer," *Investigative Radiol.*, vol. 47, no. 1, pp. 41–48, 2012.

[234] J. Oosterbroek *et al.*, "Comparison of DCE-CT models for quantitative evaluation of Ktrans in larynx tumors," *Phys. Med. Biol.*, vol. 60, no. 9, pp. 3759–3773, 2015.

[235] S. R. Barnes *et al.*, "Optimal acquisition and modeling parameters for accurate assessment of low Ktrans blood brain barrier permeability using dynamic contrast enhanced MRI," *Magn. Resonance Med.*, vol. 75, no. 5, pp. 1967–1977, 2015.

[236] A. K. Heye *et al.*, "Tracer kinetic modelling for CT quantification of subtle blood brain barrier permeability," *NeuroImage*, vol. 125, pp. 446–455, 2016.

[237] Y. Cao, D. Li, Z. Shen, and D. Normolle, "Sensitivity of quantitative metrics derived from DCE-MRI and a pharmacokinetic model to image quality and acquisition parameters," *Acad. Radiol.*, vol. 17, no. 4, pp. 468–478, 2010.

[238] P. Di Giovanni *et al.*, "The accuracy of pharmacokinetic parameter measurement in CT of the breast at 3T," *Phys. Med. Biol.*, vol. 55, no. 1, pp. 121–132, 2010.

[239] A. Jena, S. B. Mehta, and S. Taneja, "Optimizing MRI scan time in the computation of pharmacokinetic parameters (Ktrans) in breast cancer

diagnosis," *J. Magn. Resonance Imag.*, vol. 38, no. 3, pp. 573–579, 2013.
[240] C. Lavini, "Simulating the effect of input errors on the accuracy of Tofts pharmacokinetic model parameters," *Magn. Resonance Imag.*, vol. 33, no. 2, pp. 222–235, 2015.
[241] R. G. P. Lopata, W. H. Backes, P. P. J. van den Bosch, and N. A. W. van Riel, "On the identifiability of pharmacokinetic parameters in dynamic contrast-enhanced imaging," *Magn. Resonance Med.*, vol. 58, no. 2, pp. 425–429, 2007.
[242] D. R. Anderson, *Model Based Inference in the Life Sciences: A Primer on Evidence*. New York, NY, USA: Springer, 2007.
[243] J. R. Ewing and H. Bagherbadian, "Model selection in measures of vascular parameters using dynamic contrastenhanced MRI: Experimental and clinical applications," *NMR Biomed.*, vol. 26, no. 8, pp. 1028–1041, 2013.
[244] C. Roberts *et al.*, "Comparative study into the robustness of compartmental modeling and model-free analysis in CT studies," *J. Magn. Resonance Imag.*, vol. 23, pp. 554–563, 2006.
[245] M. L. James and S. S. Gambhir, "A molecular imaging primer: Modalities, imaging agents, and applications," *Physiol. Rev.*, vol. 92, no. 2, pp. 897–965, 2012.
[246] I. C. Bennett and M. A. Biggar, "The role of ultrasound in the management of breast disease," *Australas J. Ultrasound Med.*, vol. 14, no. 2, pp. 25–28, 2011.
[247] S. Campbell, "Ovarian cancer: Role of ultrasound in preoperative diagnosis and population screening," *Ultrasound Obstretics Gynecol.*, vol. 40, no. 3, pp. 245–254, 2012.
[248] M. Claudon *et al.*, "Guidelines and good clinical practice recommendations for contrast enhanced ultrasound (CEUS) in the liver - update 2012: A WFUMB-EFSUMB initiative in cooperation with representatives of AFSUMB, AIUM, ASUM, FLAUS and ICUS," *Ultrasound Med. Biol.*, vol. 39, no. 2, pp. 187–210, 2013.
[249] L. Solbiati, M. Tonolini, L. Cova, and S. N. Goldberg, "The role of contrast-enhanced ultrasound in the detection of focal liver lesions," *Eur. Radiol.*, vol. 11, no. Suppl. 3, pp. E15–E26, 2001.
[250] T. Lefort *et al.*, "Correlation and agreement between contrast-enhanced ultrasonography and perfusion computed tomography for assessment of liver metastases from endocrine tumors: Normalization enhances correlation," *Ultrasound Med. Biol.*, vol. 38, no. 6, pp. 953–961, 2012.
[251] M.-X. Tang *et al.*, "Quantitative contrast-enhanced ultrasound imaging: A review of sources of variability," *Interface Focus*, vol. 1, pp. 530–539, 2011.
[252] M. E. Eichhorn *et al.*, "Vascular targeting tumor therapy. non-invasive contrast enhanced ultrasound for quantitative assessment of tumor microcirculation," *Cancer Biol. Therapy*, vol. 9, no. 10, pp. 794–802, 2010.
[253] Y.-L. Yang *et al.*, "Correlations between the time intensity parameters of contrast-enhanced ultrasound and clinical prognosis of hepatocellular carcinoma," *Clin. Imag.*, vol. 37, pp. 308–312, 2013.
[254] M. Essig *et al.*, "MR imaging of neoplastic central nervous system lesions: Review and recommendations for current practice," *Amer. J. Neurorad.*, vol. 33, no. 5, pp. 803–817, 2012.
[255] E. Kluza, D. M. Lambregts, and R. G. Beets-Tan, "Overview of functional MR, CT, and US imaging techniques in clinical use," in *Functional Imaging in Oncology*. New York, NY, USA: Springer, 2014, pp. 293–306.
[256] R. Smith-Bindman *et al.*, "Radiation dose associated with common computed tomography examinations and the associated lifetime attributable risk of cancer," *Archives Internal Med.*, vol. 169, no. 22, pp. 2078–2086, 2009.
[257] F. Stacul *et al.*, "Contrast induced nephropathy: Updated ESUR contrast media safety committee guidelines," *Eur. Radiol.*, vol. 21, no. 12, pp. 2527–2541, 2011.
[258] S. P. Li, A. R. Padhani, and A. Makris, "Dynamic contrast-enhanced magnetic resonance imaging and blood oxygenation level-dependent magnetic resonance imaging for the assessment of changes in tumor biology with treatment," *JNCI Monographs*, vol. 2011, no. 43, pp. 103–107, 2011.
[259] M. C. Schabel and D. L. Parker, "Uncertainty and bias in contrast concentration measurements using spoiled gradient echo pulse sequences," *Phys. Med. Biol.*, vol. 53, no. 9, pp. 2345–2373, 2008.
[260] L. G. Kessler *et al.*, "The emerging science of quantitative imaging biomarkers terminology and definitions for scientific studies and regulatory submissions," *Stat. Methods Med. Res.*, vol. 24, no. 1, pp. 9–26, 2015.
[261] A. Iagaru and S. S. Gambhir, "Imaging tumor angiogenesis: the road to clinical utility," *Amer. J. Roentgenol.*, vol. 201, no. 2, pp. W183–W191, 2013.
[262] R. Luechinger *et al.*, "In vivo heating of pacemaker leads during magnetic resonance imaging," *Eur. Heart J.*, vol. 26, pp. 325–327, 2005.
[263] J. A. Nyenhuis *et al.*, "MRI and implanted medical devices: basic interactions with an emphasis on heating," *IEEE Trans. Device Mater. Rel.*, vol. 5, no. 3, pp. 467–480, Sep. 2005.
[264] T. Fritz-Hansen *et al.*, "Measurement of the arterial concentration of Gd-DTPA using MRI: A step toward quantitative perfusion imaging," *Magn. Resonance Med.*, vol. 36, no. 2, pp. 225–231, 1996.
[265] A. J. Beer and M. Schwaiger, "Imaging of integrin $\alpha v\beta 3$ expression," *Cancer Metastasis Rev.*, vol. 27, no. 4, pp. 631–644, 2008.
[266] J. Bzyl *et al.*, "The high angiogenic activity in very early breast cancer enables reliable imaging with VEGFR2-targeted microbubbles (BR55)," *Eur. Radiol.*, vol. 23, no. 2, pp. 468–475, 2013.
[267] W. Cai and X. Chen, "Multimodality molecular imaging of tumor angiogenesis," *J. Nucl. Med.*, vol. 49 Suppl 2, pp. 113s–128s, 2008.
[268] W. J. Mulder *et al.*, "Early in vivo assessment of angiostatic therapy efficacy by molecular MRI," *FASEB J.*, vol. 21, no. 2, pp. 378–383, 2007.
[269] S. McDermott and A. R. Guimaraes, *Molecular Imaging of Tumor Angiogenesis*. Rijeka, Croatia: INTECH Open Access Publisher, 2012, sec. 12.
[270] *BR55 in prostate cancer: An exploratory clinical trial*, (2010). [Online]. Available: https://clinicaltrials.gov/ct2/show/NCT01253213
[271] *A pilot trial using BR55 ultrasound contrast agent in the assessment of prostate cancer*, (2015). [Online]. Available: https://clinicaltrials.gov/ct2/show/NCT02142608
[272] S. G. Schalk *et al.*, "4D spatiotemporal analysis of ultrasound contrast agent dispersion for prostate cancer localization: A feasibility study," *IEEE Trans. Ultrason. Ferroelectr. Freq. Control*, vol. 62, no. 5, pp. 839–851, May 2015.
[273] T. Bäuerle, D. Komljenovic, M. R. Berger, and W. Semmler, "Multimodal imaging of angiogenesis in a nude rat model of breast cancer bone metastasis using magnetic resonance imaging, volumetric computed tomography and ultrasound," *J. Vis. Exp.*, vol. 66, 2012, Art. no. e4178.
[274] H. Cho *et al.*, "Noninvasive multimodality imaging of the tumor microenvironment: Registered dynamic magnetic resonance imaging and positron emission tomography studies of a preclinical tumor model of tumor hypoxia," *Neoplasia*, vol. 11, no. 3, pp. 247–IN3, 2009.
[275] L. Marti-Bonmati, R. Sopena, P. Bartumeus, and P. Sopena, "Multimodality imaging techniques," *Contrast Media Mol. Imag.*, vol. 5, no. 4, pp. 180–189, 2010.
[276] A. W. Sauter, H. F. Wehrl, A. Kolb, M. S. Judenhofer, and B. J. Pichler, "Combined PET/MRI: One step further in multimodality imaging," *Trends Mol. Med.*, vol. 16, no. 11, pp. 508–515, 2010.
[277] Quantitative Imaging Biomarkers Alliance. (2007). [Online]. Available: https://www.rsna.org/uploadedFiles/RSNA/Content/Science_and_Education/QIBA/QIBA-Fact-Sheet.pdf
[278] *QIBA profile: DCE-MRI quantification v1.0 (publicly reviewed version)*, (2012). [Online]. Available: https://www.rsna.org/QIBA-Profiles-in-Development/
[279] *CT tumor volume change profile, quantitative imaging biomarkers alliance. version 2.2. publicly reviewed version*, (2012). [Online]. Available: https://www.rsna.org/QIBA-Profiles-in-Development/
[280] *DG-PET/CT UPICT, quantitative imaging biomarkers alliance. version 1.0. publicly reviewed version*, (2014). [Online]. Available: https://www.rsna.org/QIBA-Profiles-in-Development/

Authors' photographs and biographies not available at the time of publication.